# Three-dimensional instabilities of quasi-solitary waves in a falling liquid film

N. Kofman[1], S. Mergui[1,†] and C. Ruyer-Quil[2,3]

[1]UPMC Université Paris 06, Université Paris-Sud, CNRS, laboratoire FAST, bâtiment 502,
Campus universitaire, Orsay F-91405, France

[2]Université de Savoie, CNRS, laboratoire LOCIE, Savoie Technolac, Le Bourget du Lac
73376 CEDEX, France

[3]Institut Universitaire de France (IUF), France

The stability of $\gamma_2$ travelling waves at the surface of a film flow down an inclined plane is considered experimentally and numerically. These waves are fast, one-humped and quasi-solitary. They undergo a three-dimensional secondary instability if the flow rate (or Reynolds number) is sufficiently high. Rugged or scallop wave patterns are generated by the interplay between a short-wave and a long-wave instability mode. The short-wave mode arises in the capillary region of the wave, with a mechanism of capillary origin which is similar to the Rayleigh–Plateau instability, whereas the long-wave mode deforms the entire wave and is triggered by a Rayleigh–Taylor instability. Rugged waves are observed at relatively small inclination angles. At larger angles, the long-wave mode predominates and scallop waves are observed. For a water film the transition between rugged and scallop waves occurs for an inclination angle around 12°.

**Key words:** interfacial flows (free surface), solitary waves, thin films

## 1. Introduction

Falling film flows are encountered in many industrial applications and still form the state-of-the-art technology in several chemical engineering processes because of their reduced resistance to heat and mass transfer (Alekseenko, Nakoryakov & Pokusaev 1994). For instance, absorbers and generators are currently designed using falling liquid films on vertical plates whenever pressure drop in the gas phase is critical (Fujita 1993; Bo *et al.* 2010). Optimization of such apparatuses requires the knowledge and control of the wavy regime of falling liquid films as waves are well known to intensify the heat and mass transfer both at the wall and at the free surface (Frisk & Davis 1972; Bakopoulos 1980; Yoshimura, Nosoko & Nagata 1996; Rastaturin, Demekhin & Kalaidin 2006). Such a regime is characterized by the onset of a weakly disordered state organized around large-amplitude solitary waves in interaction. These waves have a tear-drop shape preceded by capillary waves and are sometimes christened 'capillary roll waves' in reference to the large recirculation

† Email address for correspondence: mergui@fast.u-psud.fr

regions that can be found in the main humps of those waves (Balmforth & Liu 2004). The onset of capillary roll waves is pointed out as a possible reason for the intensification of transfers. Indeed, the recirculation of the fluid in the hump generates an efficient mixing (Fujita 1993; Yoshimura *et al.* 1996) which enhances transfers at the free surface, whereas backflows, induced by adverse gradients of capillary pressure, occur at the front of the waves and promote the wall-to-fluid transfers through back and forth sweeping (Dietze, Leefken & Kneer 2008; Dietze, Al-Sibai & Kneer 2009).

In most cases of interest, solitary waves are three-dimensional (3D) and form either oblique solitary waves or horseshoe-like structures (Scheid, Ruyer-Quil & Manneville 2006). The transition from the Nusselt uniform film to the wavy 3D irregular state results from a series of symmetry-breaking and supercritical bifurcations that are triggered by the inlet noise through convective instabilities (Kalliadasis *et al.* 2012). As a consequence, the sequence of instabilities can be monitored by controlling the inlet signal. Liu & Gollub (1994) and Liu, Schneider & Gollub (1995), followed later on by Park & Nosoko (2003), have thus analysed the onset of secondary instabilities of the two-dimensional (2D) primary wave train leading to 3D waves. Depending on the frequency of the applied forcing at inlet, two families of waves are identified. At frequencies close to the linear cut-off frequency, slow and roughly sinusoidal waves are selected. They are nicknamed $\gamma_1$ waves following the terminology introduced by Chang, Demekhin & Kopelevitch (1993) and clarified by Scheid *et al.* (2006). At lower frequencies, fast solitary waves, or capillary roll waves are found. They are nicknamed $\gamma_2$ waves.

Waves that belong to the $\gamma_1$ family always undergo a secondary instability as reported in the experiments by Liu *et al.* (1995) and shown by Scheid *et al.* (2006) by means of a thorough Floquet stability analysis. Depending on the values of the Reynolds number and forcing frequency, the secondary instability is either 2D or 3D. Close to the threshold of primary instability, 2D subharmonic and sideband instabilities trigger the formation of 2D solitary waves (Cheng & Chang 1995). Further from the instability threshold, 3D secondary instability modes are followed by a reorganization into 3D horseshoe-shaped solitary waves. Experimentally, 3D synchronous patterns are generally observed whereas the stability analysis seems rather to point to a subharmonic mode. However, the growth rates associated with these two modes are actually close and the observation of a synchronous instability may result from the fact that experimental noise contains a larger part of in-phase modulations than out-of-phase ones.

The stability of $\gamma_2$ large-amplitude solitary waves have been considered by Liu *et al.* (1995) who performed experiments at low inclination angle ($\beta < 7°$) using water–glycerin mixtures. They observed 2D solitary wavefronts with weak transverse modulations of spanwise wavelengths much smaller than the periodicity of the primary waves. Instead, Park & Nosoko (2003) studied the transverse evolution of solitary waves in a vertically falling water film. The wavelength of the transverse perturbations was controlled by means of needles in contact with the film free surface. Park and Nosoko found that solitary waves may be unstable to perturbations of wavelengths around 2 cm. For Reynolds number $Re > 40$, these modulations distort the whole wave and evolve into 3D $\Lambda$-shaped solitons (Demekhin *et al.* 2007; Demekhin, Kalaidin & Selin 2010) in addition to a capillary instability of wavelength of approximately 3 mm appearing on the 2D deep valleys. These observations were confirmed numerically by Demekhin & Kalaidin (2007) within the frame of the integral Kapitza–Shkadov model (Shkadov 1967).
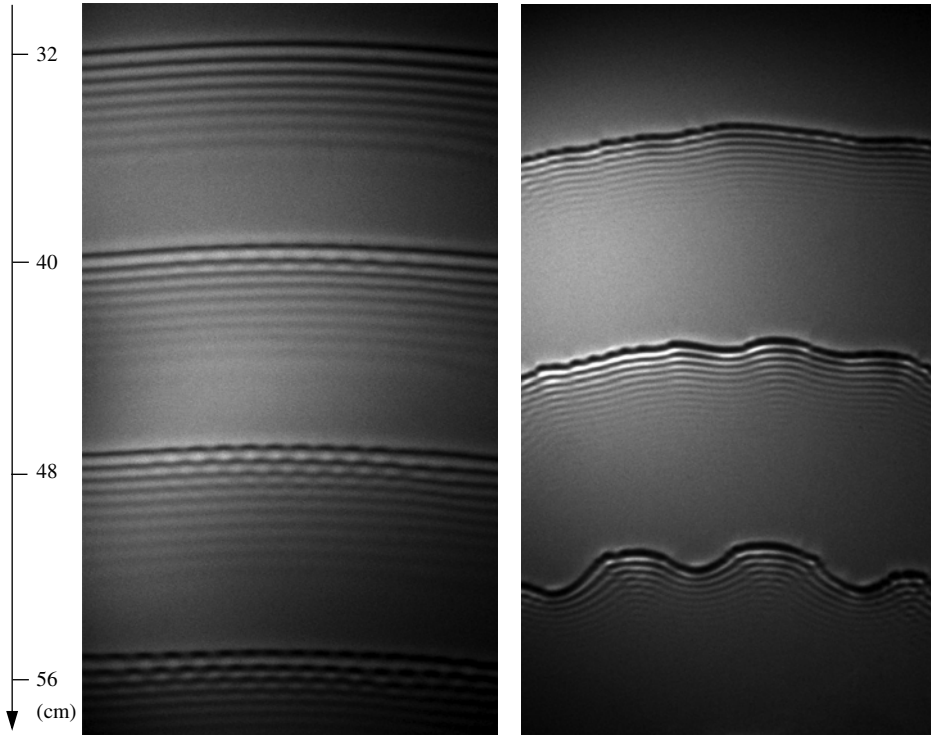
FIGURE 1. Shadowgraph pictures showing the onset of transverse 3D instabilities of a 2D quasi-solitary wave train in a water film generated by a low-frequency forcing at inlet. (*a*) The onset of rugged waves generated by a short-wave instability mode ($\beta = 8.3°$, $Re = 60$, $f = 3.5$ Hz, $\Gamma = 5975$). (*b*) Scallop waves promoted by a long-wave instability mode ($\beta = 17.9°$, $Re = 50$, $f = 4.2$ Hz, $\Gamma = 4644$). Distances are given with reference to the inlet.

In this paper, we report an experimental and numerical stability analysis of the $\gamma_2$ solitary waves focusing on the effect of the inclination angle on the secondary instability and the selection of the 3D patterns thus completing the observations by Park and Nosoko and by Liu *et al.* The starting point of our study is the discrepancy between the experimental observations at small and large inclinations which seems to point out to several different mechanisms for the secondary instability of the 2D $\gamma_2$ waves. Figure 1 illustrates two different experiments showing the onset of two different wave patterns on a water falling film. At small inclination angle (figure 1*a*), the wave crests are nearly undeformed and a weak transverse modulation is observed with a wavelength close to the length of the capillary ripples and is reminiscent of Liu and Gollub's observations. These rugged waves exhibit a rough or rugged capillary region. At large inclination angle (figure 1*b*), similarly to Park and Nosoko's observations, the transverse wavelength is much larger than the typical length of the capillary bow waves. The 3D modulated waves have a festooned or scalloped shape and are hereinafter referred to as scallop waves. This calls for a distinction between a 'long-wave' and a 'short-wave' instability mode and the study of the transition between the two.

The paper is organized as follows. Section 2 introduces dimensionless parameters and recalls the low-dimensional models derived by Ruyer-Quil & Manneville (2000)

and Scheid *et al.* (2006), as well as the Floquet analysis of 2D waves that is detailed in Scheid *et al.* (2006). Then, an energy budget of the perturbations is introduced with the aim of identifying the physical mechanisms at work in both long- and short-wave instability modes. The experimental set-up and the measuring techniques are described in §3 and results are presented in §4. A discussion follows in §5. Section 6 concludes the present work.

## 2. Numerical tools

### 2.1. *Formulation*

We consider a liquid film falling down an inclined plane making an angle $\beta$ with the horizontal plane. The surrounding gas is assumed to be passive, that is at rest with a constant and uniform pressure and exerting no shear stresses on the free surface. Physical properties of the liquid are assumed to be constant. Quantities $\rho$, $\mu$, $\nu = \mu/\rho$ and $\sigma$ refer to the density, dynamic and kinematic viscosities and surface tension, respectively. Coordinate $x$ is oriented in the streamwise direction, while $y$ refers to the cross-stream coordinate, i.e. perpendicular to the plane, and $z$ is the transverse direction. Accordingly, $e_x$, $e_y$ and $e_z$ stand for the unit vectors, so that the gravitational acceleration reads $g = g \sin \beta e_x - g \cos \beta e_y$. Finally, the velocity field is denoted by $u = u e_x + v e_y + w e_z$.

Flow conditions are parametrized by three characteristic lengths, the inlet film thickness $\bar{h}_N$, a viscous-gravity length $l_\nu = \nu^{2/3}(g \sin \beta)^{-1/3}$ and a capillary length $l_c = \sqrt{\sigma/(\rho g \sin \beta)}$, from which the Reynolds $Re$ and Kapitza numbers $\Gamma$ are defined as

$$Re = \frac{g \sin \beta \bar{h}_N^3}{3\nu^2} = \frac{1}{3}\left(\frac{\bar{h}_N}{l_\nu}\right)^3 \quad \text{and} \quad \Gamma = \frac{\sigma}{\rho \nu^{4/3}(g \sin \beta)^{1/3}} = \left(\frac{l_c}{l_\nu}\right)^2. \qquad (2.1a,b)$$

The set of dimensionless groups is completed by the inverse slope $\cot \beta$ which defines the geometry of the flow. The inlet film thickness is related to the inlet flow rate per unit span $\bar{q}_N$ by the Nusselt flat-film solution

$$u(y) = \frac{g \sin \beta}{\nu}\left(y\bar{h}_N - \frac{1}{2}y^2\right), \qquad (2.2)$$

which corresponds to the balance of gravity and viscosity. Therefore, the aforementioned Reynolds number is proportional to the inlet flow rate as $Re = \bar{q}_N/\nu$. Lastly, note that the Kapitza number depends only on the liquid properties and the inclination of the plane. As a consequence, once the working liquid and geometry are set, free parameters are reduced to the sole Reynolds number $Re$.

Governing equations consist of the Navier–Stokes equations augmented with the free-surface kinematic and shear-free boundary conditions, and the Laplace law (see, for instance, Heining, Pollak & Aksel 2012). Hereinafter, experimental results are discussed with respect to the results from a reduced set of equations, or a model, that has been obtained using the long-wave nature of the instability and after elimination of the cross-stream coordinate $y$. Two main reasons support this choice. (i) Reduced sets of equations enable a comprehensive stability analysis at an affordable computational cost. (ii) Models give access to the 'pith and marrow' of the flow dynamics. In particular, they offer a convenient framework to identify the origins and physical mechanisms of the instability modes.

## 2.2. *WRIBL model and Shkadov's notation*

The starting point of the reduction of the governing set of equations is the introduction of a film parameter $\epsilon$, which compares the typical length of the waves to the thickness of the film. Slow time and space modulations are assumed in the in-plane directions, which reads $\partial_t, \partial_x, \partial_z \sim \epsilon \ll 1$. Truncation at $O(\epsilon^2)$ of the governing equations thus enables us to eliminate the *y*-projection of the momentum equation and to eliminate the pressure field. The resulting equations are analogous to the Prandtl equations in boundary-layer theory (Schlichting, Gersten & Krause 2004; Kalliadasis *et al.* 2012), and the former are usually referred to as the boundary-layer approximation. Assuming $O(\epsilon)$ deviations from the parabolic velocity profile (2.2) of the flat-film solution, and averaging the continuity equation and the momentum balance across the film layer with an appropriately chosen weight thus yields (Ruyer-Quil & Manneville 2000; Scheid *et al.* 2006, 2008):

$$\partial_t h = -\nabla \cdot \boldsymbol{q}, \tag{2.3a}$$

$$
\begin{aligned}
\delta \partial_t \boldsymbol{q} = {}& \delta \left[ \frac{9}{7} \left( \frac{\boldsymbol{q} \cdot \nabla h}{h^2} - \frac{\boldsymbol{q}}{h} \cdot \nabla \right) \boldsymbol{q} - \frac{8}{7} \frac{\nabla \cdot \boldsymbol{q}}{h} \boldsymbol{q} \right] + \frac{5}{6} h \left( \boldsymbol{e}_x - \zeta \nabla h + \nabla \nabla^2 h - 3 \frac{\boldsymbol{q}}{h^3} \right) \\
& + \eta \left[ \frac{7}{2} h \nabla \cdot \left( \frac{\nabla \boldsymbol{q}^T}{h} \right) + h \nabla \cdot \left( \frac{\nabla \boldsymbol{q}}{h} \right) + \frac{13}{4} \frac{\boldsymbol{q} \cdot \nabla h}{h^2} \nabla h + \frac{3}{4} \frac{\nabla h \cdot \nabla h}{h^2} \boldsymbol{q} \right. \\
& \left. - \frac{73}{16} \left( \frac{\boldsymbol{q}}{h} \cdot \nabla \right) \nabla h - \frac{23}{16} \frac{\nabla^2 h}{h} \boldsymbol{q} + \frac{13}{16} \left( \frac{\nabla h}{h} \cdot \nabla \boldsymbol{q} - \frac{\nabla \cdot \boldsymbol{q}}{h} \nabla h \right) \right].
\end{aligned}
\tag{2.3b}
$$

Equations (2.3) are a set of evolution equations for the film thickness $h$ and the flow rate $\boldsymbol{q} = q\boldsymbol{e}_x + p\boldsymbol{e}_z = \int_0^h u\boldsymbol{e}_x + w\boldsymbol{e}_z \, \mathrm{d}y$. The variables $h$ and $\boldsymbol{q}$ can be identified with the mass and momentum of a fluid column of infinitesimal cross-section. As such, (2.3a) is the exact mass balance, and (2.3b) is the approximate momentum balance that governs the evolution of the said liquid column. Throughout (2.3), the notation of the in-plane Del operator has been unambiguously simplified to the symbol $\nabla = \partial_x \boldsymbol{e}_x + \partial_z \boldsymbol{e}_z$. Using Einstein notation where $\boldsymbol{e}_{1,2} = \boldsymbol{e}_{x,z}$ and $x_1 = x$ and $x_2 = z$, the gradient, divergence and material derivative read $\nabla \boldsymbol{q} = \partial_j q_i \boldsymbol{e}_i \otimes \boldsymbol{e}_j$, $\nabla \cdot (\nabla \boldsymbol{q}/h) = \partial_j \left( \partial_j q_i/h \right) \boldsymbol{e}_i$ and $\boldsymbol{q} \cdot \nabla \boldsymbol{q} = q_j \partial_j q_i \boldsymbol{e}_i$ (Germain 1973).

Because of its analogy with the Kármán–Polhausen approximation in boundary-layer theory, (2.3) is referred to as the two-equation weighted-residual integral boundary-layer (WRIBL) model (Oron, Gottlieb & Novbari 2007). Equations (2.3) have been written using Shkadov's notation (Shkadov 1977; Scheid *et al.* 2006), which makes apparent the separation of scales between the 'fast' cross-stream variable $y$ and the slow ones $x$ and $z$ by introducing a 'compression factor' $\kappa = (l_c/\bar{h}_N)^{2/3}$, which is adjusted by balancing the body force that sets the fluid into motion, i.e. $\rho g \sin \beta$, with the capillary pressure gradient $\propto \sigma \partial_{xxx} h$. The length scales in the $x$ and $z$ directions are thus taken as $\kappa \times \bar{h}_N$, where the inlet film thickness $\bar{h}_N$ stands for the length scale in the cross-stream $y$ direction; accordingly, the timescale is taken as $\nu \kappa /(g \bar{h}_N \sin \beta)$.

Shkadov's scales introduce three dimensionless groups. Namely, a reduced Reynolds number, $\delta$, a reduced slope, $\zeta$, and a 'viscous dissipation number', $\eta$:

$$\delta \equiv \frac{3Re}{\kappa}, \quad \zeta \equiv \frac{\cot \beta}{\kappa} \quad \text{and} \quad \eta \equiv \frac{1}{\kappa^2} = \left( \frac{\bar{h}_N}{l_c} \right)^{4/3}. \tag{2.4a–c}$$

The reduced Reynolds number $\delta$ combines inertia, viscosity and surface tension into a single parameter. It measures inertia versus viscous effects at the scale $\kappa \bar{h}_N$ defined by

the balance of gravity and surface tension. The viscous diffusion parameter has been recast in (2.4) in terms of the length ratio $\bar{h}_N/l_c$ and thus compares surface tension to the streamwise viscous effects, or Trouton viscosity (Ribe 2001). It measures the efficiency of the damping of short waves by viscous diffusion as compared to the damping by surface tension. In most cases $\eta$ is small as the capillary length is generally much larger than the film thickness, which is a prerequisite to the long-wave assumption. As a consequence, Trouton viscous effects are often dropped out ($\eta \to 0$) and the set of parameters is reduced to $\delta$ and $\zeta$ only. Finally, Shkadov's scales have the advantage to unfold the physical origin of the different terms appearing in the averaged momentum balance (2.3b). Thus, inertia effects and viscous-dispersion effects are associated with $\delta$ and $\eta$, respectively.

The WRIBL model (2.3) is consistent up to $O(\epsilon)$ for inertial terms and up to $O(\epsilon^2)$ for viscous terms. This inconsistency can be eliminated but at the cost of a more complex formulation. However, the WRIBL model has been validated through direct comparisons with the experiments by Alekseenko, Nakoryakov & Pokusaev (1985), Liu & Gollub (1994) and Liu *et al.* (1995) in the 2D and 3D flow regimes. To the best of the authors' knowledge, this model is the simplest one which satisfactorily reproduces the wavy dynamics of falling films, capturing the instability onset, the nonlinear 2D dynamics and its evolution to the fast $\gamma_2$ waves, as well as the 3D instability of the slow $\gamma_1$ waves (Ruyer-Quil & Manneville 2000; Scheid *et al.* 2006).

### 2.3. *Two-dimensional solitary wave*

Fast 2D $\gamma_2$ travelling-wave solutions to (2.3) are looked after. Such waves are periodic, spanwise independent ($\partial_z = 0$, $p = 0$) and move at a constant speed and shape. The system of partial differential equations (2.3) reduces to ordinary differential equations (o.d.e.s) in the moving frame of reference, $\xi = x - ct$, where $c$ refers to the phase speed of the waves. Integration of the mass balance yields $q = ch + q_{mov}$ where $q_{mov} = \int_0^h (u - c)\mathrm{d}y$ is the conserved flow rate in the moving frame. After elimination of the mass flux, one is led to a single o.d.e. which is next recast as an autonomous dynamical system in a 3D phase space spanned by $h$, $\mathrm{d}h/\mathrm{d}\xi$ and $\mathrm{d}^2h/\mathrm{d}\xi^2$. The constant $q_{mov}$ is determined by maintaining the averaged flow rate to its value for the Nusselt flat-film solution, which reads $\langle q \rangle = 1/3$ where $\langle \cdot \rangle = L_x^{-1} \int_0^{L_x} (\cdot)\,\mathrm{d}\xi$ and $L_x$ is the period. This condition enables to relate our computations to the travelling waves observed in experiments as a response to the periodic excitation at inlet (Scheid *et al.* 2005).

In practice, we have extensively used the software AUTO-07P (Doedel 2008) and constructed travelling-wave branches of solutions by continuation starting from Hopf bifurcations and increasing the period $\Lambda$. Period-doubling bifurcations were detected by duplicating the initial solution and doubling the period. The procedure is detailed in Scheid *et al.* (2006) and Kalliadasis *et al.* (2012). In the case of multiplicity of solutions for a given frequency $c/\Lambda$, we have selected the fastest one, or 'dominant wave', as they systematically supersede slower waves when integration in time is considered (Shkadov & Sisoev 2004).

### 2.4. *Three-dimensional stability analysis*

We consider here the stability of 2D solutions ($h_0(\xi)$, $q_0(\xi) = ch_0(\xi) + q_{mov}$) with respect to transverse perturbations. We have performed a standard Floquet analysis of the wave against spanwise modulations. The procedure is similar to that followed by Scheid *et al.* (2006) and is therefore simply sketched below.

Denoting by $X$ the vector formed by the three unknowns $h$, $p$ and $q$, we superpose to a 2D solution $X_0(\xi, z, t)$ a small perturbation $\epsilon X_1(\xi, z, t)$ where $\epsilon \ll 1$. The perturbation $X_1$ is decomposed into a sum of planar waves $\sum_{\varphi, k_z} X_p(\xi, z, t)$ with $X_p = (h_p, q_p, p_p) = \tilde{X}(\xi) \exp\{i\varphi k_x \xi + i k_z z + \lambda t\}$. Here $\tilde{X}$ is periodic in $\xi$ with period $L_x$, $k_x = 2\pi/L_x$ is the wavenumber of the 2D basic stationary wave, $k_z$ is the real wavenumber of the transverse perturbation, and i refers to the imaginary unit. The detuning parameter, $\varphi$, is the ratio of the streamwise wavenumber of the perturbation. The analysis is therefore not limited to the stability of a single wave but encompasses every perturbation to an infinite periodic wave train. Substitution into (2.3$b$) yields a linear eigenvalue problem, formally written

$$\lambda \tilde{X} = \mathscr{L}_{\varphi, k_z} (X_0; \varphi, k_z) \tilde{X}, \tag{2.5}$$

where $\mathscr{L}_{\varphi, k_z}$ stands for a linear differential operator parametrized by $\varphi$ and $k_z$. Equation (2.5) is solved numerically with a pseudo-spectral algorithm (see appendix A). Symmetries, i.e. reflexion in the spanwise direction and conjugation, enable us to limit the parameter space to $\varphi \in [0, 1/2]$ and $k_z \in [0, \infty]$. However, for most of the $\gamma_2$ waves that have been considered, the wavelength is sufficient to limit the interaction between succeeding solitary-like waves and the most amplified mode at a given transverse wavenumber $k_z$ is not affected by the value of $\varphi$. The results of the stability analysis of a single solitary-like wave, that is of a wave confined to a periodic domain matching its length ($\varphi = 0$), are close to those corresponding to the stability of an infinite wave train ($\varphi \neq 0$), which reduces the range of parameters to $k_z \in [0, \infty[$.

## 2.5. *Energy budget*

We adapt the energy budget introduced by Spaid & Homsy (1996) and Skotheim, Thiele & Scheid (2003), who interpreted the growth rate $\lambda$ as an energy production rate and defined a quadratic form to compute the different contributions to this production rate. The linear system (2.5) consists of a linearized kinematic balance

$$\lambda \tilde{h} = i k_x \varphi (c \tilde{h} - \tilde{q}) + c \tilde{h}' - \tilde{q}' - i k_z \tilde{q} \equiv \mathscr{L}_{\varphi, k_z}^{Kin} \tilde{X}, \tag{2.6}$$

where the primes refer to the derivatives with respect to $\xi$, and a linearized momentum balance, written formally as

$$\lambda \tilde{q} = \mathscr{L}_{\varphi, k_z}^{Mom} (X_0; \varphi, k_z) \tilde{X}, \tag{2.7}$$

where $\tilde{q} = (\tilde{q}, \tilde{p})$.

Following Spaid & Homsy (1996), we define the energy of deformation $E_d$ associated with a planar wave as

$$E_d = \tfrac{1}{2} \langle h_p, h_p \rangle = \tfrac{1}{2} \langle \tilde{h}, \tilde{h} \rangle e^{2\lambda_r t}, \tag{2.8}$$

where the inner product is defined as $\langle X, Y \rangle = L_x^{-1} \int_0^{L_x} X Y^\star d\xi$, the star referring to transpose conjugation. The variation of the energy of deformation is given by

$$\frac{dE_d}{dt} = \lambda_r \langle h_p, h_p \rangle = 2\lambda_r E_d, \tag{2.9}$$

where the growth rate $\lambda_r$ is the real part of $\lambda$.

The growth rate can be computed from the linearized kinematic balance (2.6) as

$$\lambda_r = Re\left(\langle \mathscr{L}^{Kin}_{\varphi,k_z}\tilde{X}, \ \tilde{h}\rangle\right)/\langle\tilde{h}, \ \tilde{h}\rangle. \tag{2.10}$$

From (2.9), the growth rate $\lambda_r$ can thus be identified with a production rate of the energy of deformation induced by a planar wave, whose contributions would be either the divergence of the perturbation flux in the direction of the flow, i.e. $\langle ik_x\varphi(c\tilde{h} - \tilde{q}) + c\tilde{h}' - \tilde{q}', \ \tilde{h}\rangle$, or in the transverse direction, $\langle -ik_z\tilde{q}, \ \tilde{h}\rangle$.

However, (2.10) provides little access to the origin of the instability and its mechanisms. We thus rather focus on the linearized momentum balance (2.7) and write instead

$$\lambda_r = Re\left(\langle \mathscr{L}^{Mom}_{\varphi,k_z}\tilde{X}, \ \tilde{q}\rangle\right)/\langle\tilde{q}, \ \tilde{q}\rangle = \sum \lambda_n, \tag{2.11}$$

which can be identified with the rate of production of the kinetic energy associated with the considered planar wave

$$E_k = \frac{1}{2}\langle q_p, \ q_p\rangle, \quad 2\lambda_r = \frac{1}{E_k}\frac{\mathrm{d}E_k}{\mathrm{d}t}, \quad \text{with } q_p = (q_p, p_p). \tag{2.12a,b}$$

Equation (2.11) can thus be interpreted as a kinetic energy budget, whose contributions $\lambda_n$ are listed in appendix B and grouped with respect to their physical origin (inertia, drag, 'Trouton' viscosity, surface tension, hydrostatic pressure) and whether they emanate from the projections of the linearized momentum balance in the $x$ or $z$ directions.

## 3. Experimental set-up

### 3.1. *Description of the set-up*

The experimental apparatus is shown in figure 2. It consists in an inclined glass plate (150 cm × 37 cm) placed on a massive framework mounted on rubber feet to reduce the influence of environmental vibrations. The inclination angle can be changed in the range 0–20°. A gear pump brings the liquid from a collection tank located at the exit of the plane to an upstream tank from which it emerges and flows down the plane. This upstream tank is filled with several glass sphere layers in order to homogenize the entering flow. A temporal forcing of the film is introduced at the inlet to trigger 2D reproducible solitary waves. An aluminum plate is fixed to the membrane of two loudspeakers and generates harmonic vibrations above the liquid surface on the whole width of the upstream tank. Water, water–glycerin and butanol solutions are used as working fluid. The mass flow rate is measured by weighting at the exit and the temperature and density of the liquid are controlled during the experiments. Experimental parameters and their range of variation are specified in table 1. The wave patterns are visualized by illuminating the liquid film with oblique white light and by observing from above with a 2D camera to provide shadow images. The Schlieren method developed by Moisy, Rabaud & Salsac (2009), described in detail in the next subsection, is used to measure the film thickness.

### 3.2. *Schlieren method*

Three-dimensional wavy patterns are characterized by instantaneous measurement of the film thickness over an area of typical 10 cm × 10 cm extension using a
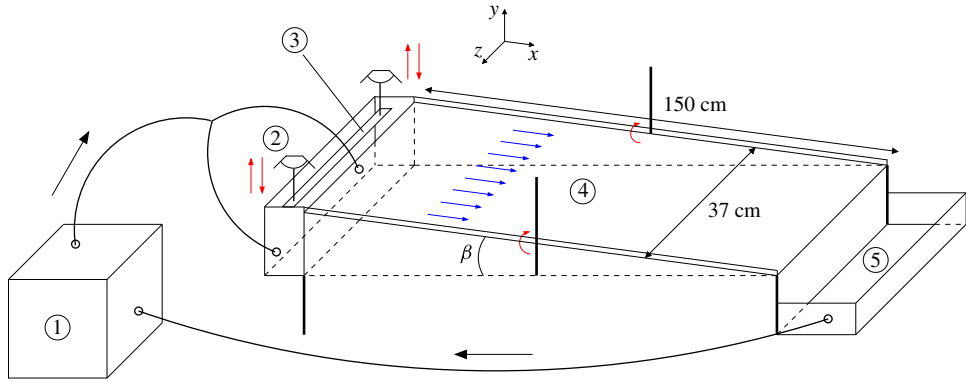
FIGURE 2. (Colour online) Sketch of the experimental set-up: 1, pump; 2, loudspeakers; 3, aluminium plate; 4, glass plate; 5, collection tank.

| Physical parameter | Notation | Domain of variation |
|---|---|---|
| Density | $\rho$ | 998–1082 kg m$^{-3}$ |
| Kinematic viscosity | $\nu$ | $1$–$2.8 \times 10^{-6}$ m$^2$ s$^{-1}$ |
| Surface tension | $\sigma$ | 49–72 mN m$^{-1}$ |
| Temperature | $T$ | 18–23 °C |
| Kapitza number | $\Gamma$ | 1971–7213 |
| Inclination angle | $\beta$ | 5–18° |
| Volumetric flow rate | $Q$ | 0–130 l h$^{-1}$ |
| Reynolds number | $R$ | 0–60 |
| Frequency | $f$ | 3–9 Hz |

TABLE 1. Experimental parameters (water, water–glycerine and butanol mixtures).

Schlieren Synthetic method. This method is based on the analysis of a refracted image of a dot pattern visualized through a liquid/air interface and is applicable if the surface curvature is weak in order to prevent ray crossings. Under restrictive conditions (weak slope approximation and weak amplitude approximation), the surface gradient is proportional to the apparent displacement field seen by a camera located far from the dot-pattern. A numerical integration based on a least-squares inversion of the gradient operator is employed for the reconstruction of the surface height (Moisy *et al.* 2009). While Moisy *et al.* (2009) were always in the situation where a reference state corresponding to a flat interface is easily available, in the falling film problem we do not have access to the unstable reference state with the same mean height $h_0$ than the deformed state. Additional measurements are thus required to obtain absolute values of the thickness. We used a needle mounted on a microscopic translation stage to measure the absolute maximum amplitude of the waves. The reconstructed height field is rescaled *a posteriori* by adjusting the mean thickness $h_0$ such that the maximum calculated by the Schlieren method corresponds to the needle measurement.

In practice, the dot pattern is located just behind the glass plate. The camera is placed at a distance $H \sim 140$ cm from the dot pattern and the typical visualized field length is $L \sim 10$ cm. The maximum paraxial angle is given by $\theta_{max} = L/(\sqrt{2}H) \sim 0.05 \sim 3°$ which is sufficiently low to assure a negligible paraxial distortion. Within

the weak slope approximation, the surface gradient $\nabla h$ is directly proportional to the displacement field $\delta r$ of the dots:

$$\nabla h = - \left( \frac{1}{(1 - 1/n_l) \; h_p} - \frac{1}{H} \right) \delta r, \qquad (3.1)$$

where $n_l$ is the refractive index of the liquid and $h_p$ is the effective pattern-surface distance which is related to the film thickness $h$ by the formula:

$$h_p = h + \frac{n_l}{n_g} h_g. \qquad (3.2)$$

Here, $n_g$ and $h_g$ stand for the refractive index and the thickness of the glass plate, respectively. Under the weak amplitude approximation, $h \sim h_0$, and (3.1) is simply linear.

In our experiments, $h_0 \sim 0.5$ mm and the surface height lies in the range 0.2–0.8 mm. The weak amplitude approximation is not well verified. However, consequences on the slope calculation remain acceptable since the second term of (3.2) is much greater than $h$ ($n_l = 1.33$, $n_g = 1.52$ and $h_g = 5.9$ mm). The maximum slope magnitude calculated from (3.1) is approximately 0.3 providing an error less than 1 % compared with the nonlinearized case. The weak slope approximation is thus valid in our configuration. The accuracy of the method applied to our configuration can be estimated to yield an error of 20 µm. The spatial resolution depends on the camera resolution, the field size and the dot-pattern characteristics and is estimated to be around 0.5 mm. The temporal resolution is directly related to the acquisition rate of the camera, which varies from 100 to 500 Hz.

In addition, a one-point temporal measurement based on a CCI (confocal chromatic imaging) technique has been performed. The principle of the CCI technique is to focus a polychromatic point light using a biconvex lens which provides a continuum of monochromatic images of the point source due to its chromatic aberration. A pinhole collects the light originating from a reflecting interface placed in the continuum, which is then analysed by a spectrometer. The location of the interface is then deduced from a calibration curve. The sensor model used in our experiments (Micro-Epsilon IFS2403-10) allows for the detection of the air–water interface location with a precision of 1 µm and a temporal resolution in the range 0.1–10 kHz but does not directly measure the thickness of the film as the probe cannot detect the water–glass interface.

## 4. Results

### 4.1. *Validation of the Schlieren method*

Figure 3 displays the wave profiles of 2D travelling waves generated by a periodic forcing at inlet. After an initial linear growth, the wave amplitude rapidly saturates and periodic 2D waves emerge with a frequency corresponding to the applied inlet forcing. Time records shown in figure 3(*a*) and (*b*) and obtained using the Schlieren and CCI techniques are typical of the $\gamma_1$ and $\gamma_2$ slow and fast waves that had been also observed by Liu & Gollub (1994). The $\gamma_1$ waves are nearly sinusoidal for their rounded crests and sharp troughs. The $\gamma_2$ waves displayed in figure 3(*b*) exhibit a large-amplitude tear-drop hump preceded by capillary ripples. This separation into two regions, a hump region and a capillary region, which characterizes $\gamma_2$ waves, is
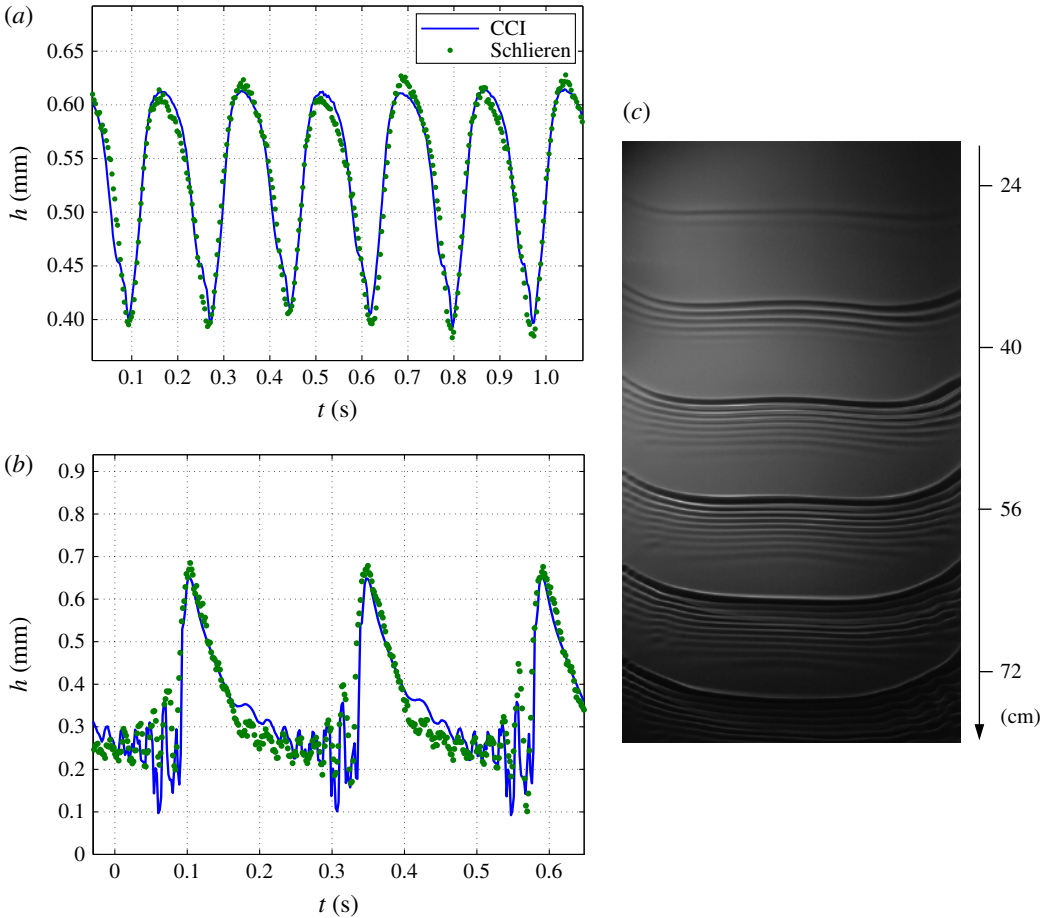
FIGURE 3. (Colour online) (*a,b*) Validation of the Schlieren method by comparison with CCI measurements; the distance from inlet is $x = 35$ cm: (*a*) $\gamma_1$ waves, $\beta = 5.2°$, $Re = 37$, $f = 5.7$ Hz, $\nu = 1.03 \times 10^{-6}$ m$^2$ s$^{-1}$, $\Gamma = 7213$; (*b*) $\gamma_2$ waves, $\beta = 10.2°$, $Re = 42$, $f = 4.1$ Hz, $\nu = 1.00 \times 10^{-6}$ m$^2$ s$^{-1}$, $\Gamma = 6018$. (*c*) View from above showing the curvature of solitary wavefronts for a water–glycerine mixture ($\beta = 7.9°$, $Re = 35$, $f = 3.2$ Hz, 34 %, $\nu = 2.8.10^{-6}$ m$^2$ s$^{-1}$, $\Gamma = 1448$).

made possible by the large ratio between the spatial extension of the hump and the typical length of the capillary ripples. In experiments conducted with water–glycerin mixtures, well-separated waves, i.e. waves separated by a flat film are generally observed as shown in figure 3(*c*) or from Liu and Gollub's results (Liu & Gollub 1994), because capillary waves are efficiently damped by elongational viscosity. As the current experiments are mainly performed with water as working fluid, the film is never flat between two waves and 2D $\gamma_2$ waves are not strictly solitary as capillary ripples tend to accumulate between successive humps. Yet, as a convenience, we refer to them hereinafter as quasi-solitary waves.

Due to the regularity of the 2D travelling-wave trains, the accuracy of the Schlieren method is estimated by comparisons with respect to the local temporal CCI technique. The two techniques provide close results when $\gamma_1$ waves are encountered. Agreement is somewhat less satisfactory in the case of $\gamma_2$ waves. However, the minimum and
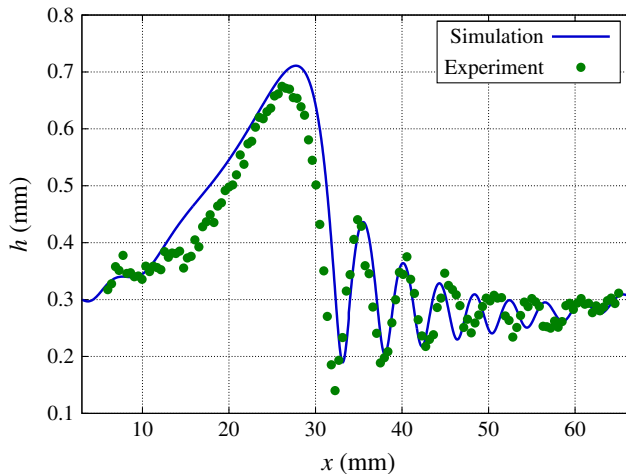
FIGURE 4. (Colour online) Comparison between a Schlieren measurement and the 2D stationary solution obtained by continuation. The experimental parameters are: $\beta = 10.2°$, $Re = 42$, $f = 4.1$ Hz, $\nu = 1.00 \times 10^{-6}$ m$^2$ s$^{-1}$, $\Gamma = 6018$.

maximum heights as well as the amplitude, spatial distribution and lengths of the capillary ripples are well captured by the Schlieren method, which gives us confidence in its accuracy. The observed discrepancy is mainly due to the technical impossibility of recording temporal signals of the free-surface elevation simultaneously at exactly the same distance from the side edge of the plane. Indeed, the two signals displayed in figure 3(*b*) have been recorded at two different locations spaced 3 cm apart in the transverse direction. This small shift in the measuring locations can however be significant as 2D waves have a tendency to present a non-negligible curvature (Leontidis *et al.* 2010), as illustrated in figure 3(*c*). As a result, the capillary region of $\gamma_2$ waves is slightly modulated in the transverse direction, which may be sufficient to explain the slight disagreement between the records shown in figure 3(*b*). It should be mentioned, however, that the sidewall effects on the onset of the primary instability are weak in the range of inclination angles under study (Vlachogiannis *et al.* 2010). Furthermore, according to Leontidis *et al.* (2010), the wave curvature decreases drastically as the forcing frequency, $f$, is raised, and to a lesser extent as the Reynolds number, *Re*, increases. In the current paper $f > 3$ Hz and $Re > 35$ leading to relatively small final curvatures. In all of the experiments the 2D basic state consists in a fully developed 2D solitary waves moving with a constant phase speed and 3D patterns are triggered in the centre part of the channel where the fronts are slightly curved as shown in figure 1.

We next question the reliability of the two-equation model (2.3) to capture the characteristics of $\gamma_2$ waves satisfactorily. Figure 4 compares experimental profiles obtained with the Schlieren method to travelling-wave solutions given by the model. The comparison is satisfactory as both the wave peak height (710 µm for the experiments and 670 µm for the simulation) and the wave velocity (26.2 and 24.2 cm s$^{-1}$) are well reproduced by the simulation. The shape of the capillary waves region is also very similar even though the model predicts one more capillary wave in this case.
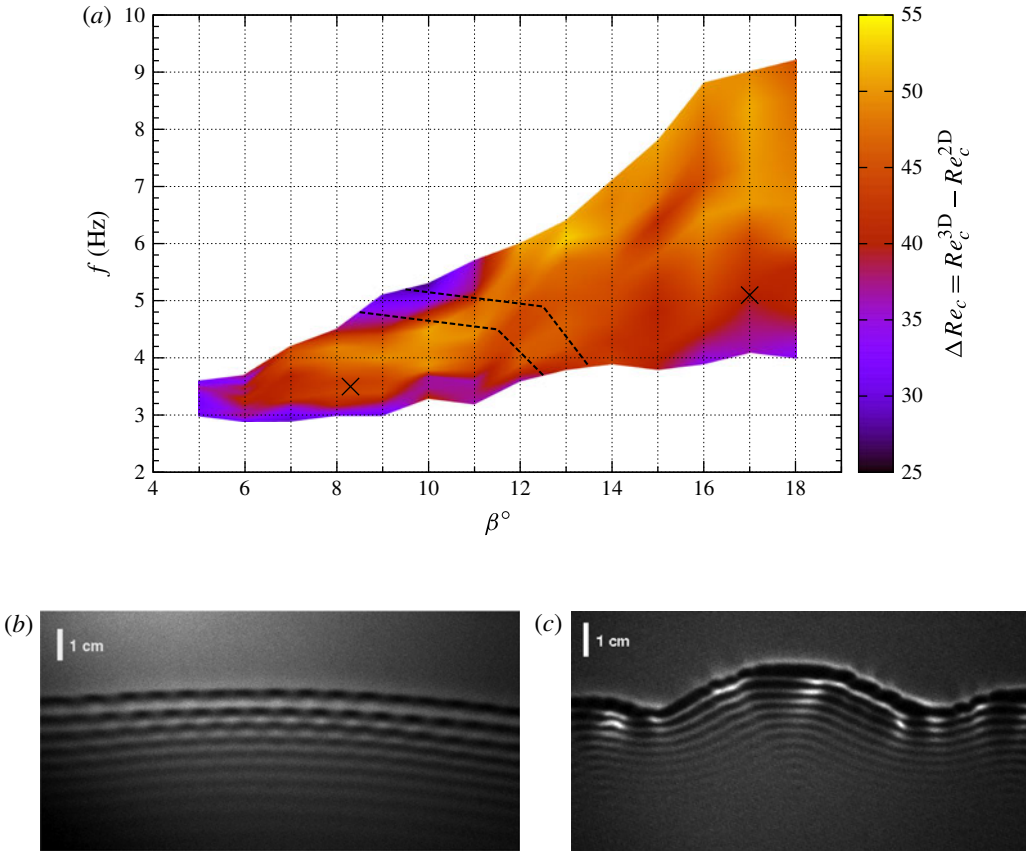
FIGURE 5. (Colour online) Three-dimensional instability of $\gamma_2$ solitary waves. Fluid is water ($\nu = 1.08 \times 10^{-6}$ m$^2$ s$^{-1}$). (*a*) Threshold of the 3D secondary instability in the $\beta$–$f$ plane. The gap between the thresholds of the primary 2D and secondary 3D instabilities, $\Delta Re_c = Re_c^{3D} - Re_c^{2D}$, is represented as a colour map. The dashed lines delimit regions where a short-wave instability mode (small inclination angle $\beta$) or a long-wave instability mode (large $\beta$) is observed. Associated shadowgraphs of rugged waves and scallop waves are shown in subfigures (*b,c*), respectively. Parameters are $\beta = 8.3°$, $f = 3.5$ Hz and $\beta = 17°$, $f = 5.1$ Hz, respectively, corresponding to the two crosses depicted in (*a*).

## 4.2. *Stability diagram of solitary waves*

The stability of 2D $\gamma_2$ solitary waves with respect to transverse perturbations depends on the Reynolds number, or perhaps more precisely, on the distance from the instability threshold $\Delta Re = Re - Re_c^{2D}$, where $Re_c^{2D} = \frac{5}{6} \cot \beta$ is the critical Reynolds number for the onset of the primary instability (Benjamin 1957). In line with the findings by Liu *et al.* (1995) and Leontidis *et al.* (2010), 2D $\gamma_2$ waves remain stable to transverse secondary perturbations below a certain critical Reynolds number $Re_c^{3D}$, which is a function of the geometry (inclination angle $\beta$) and the shape of the 2D wave train (forcing frequency $f$). Figure 5(*a*) presents an estimate of $Re_c^{3D}$ based on our experimental findings in the plane $f$ versus $\beta$. The experimental procedure used to find $Re_c^{3D}$ is as follows: first, at a given inclination angle, the flow rate is adjusted such that $Re = Re_c^{2D} + \Delta Re$ with a moderate value of $\Delta Re$. The frequency range over which 2D solitary waves are triggered is then identified. In fact, this range is rather
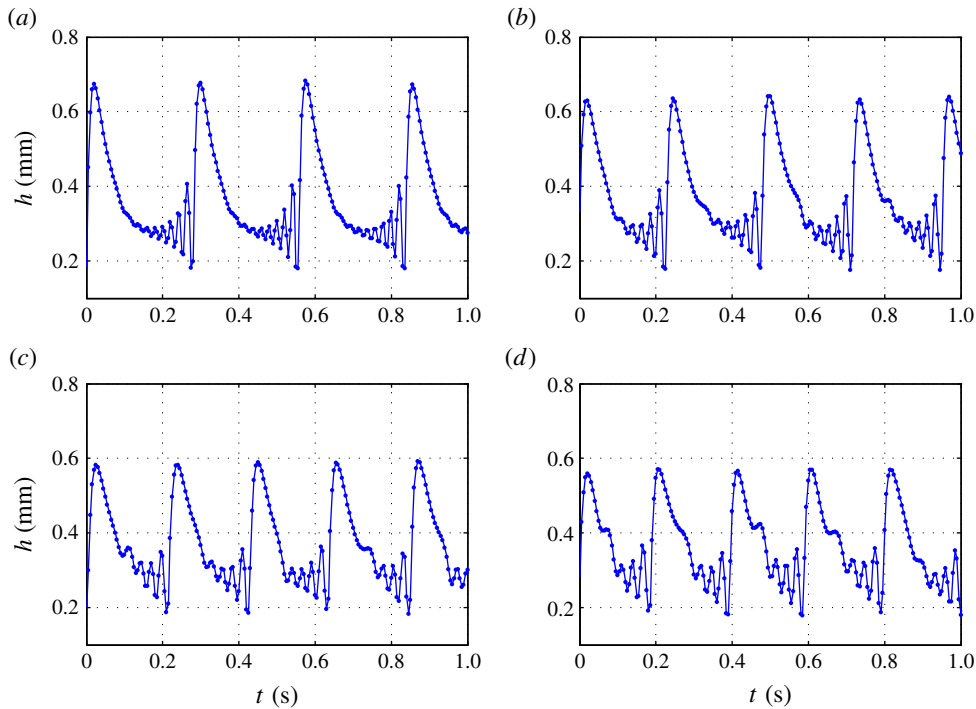
FIGURE 6. (Colour online) Time records of the film height from CCI measurements at different forcing frequencies $f$ (($a$) $f = 3.6$ Hz; ($b$) $f = 4.2$ Hz; ($c$) $f = 4.7$ Hz; ($d$) $f = 5.0$ Hz). Here $Re = 34$ and $\beta = 10°$. Fluid is water ($\nu = 1.08 \times 10^{-6}$ m$^2$ s$^{-1}$).

limited. Indeed, at low frequencies, the long-wave nature of the primary instability weakens the response of the flow to the inlet forcing, as the spatial growth rate goes to zero along with the forcing frequency. As a result, synchronization of the flow requires levels of the inlet excitation amplitude that are not achievable using the forcing device adopted in the experimental set-up. At high frequencies, either the flow does not respond to the applied periodic forcing and the natural disordered evolution of the film is observed, or $\gamma_1$ slow wave trains are selected (already studied by Scheid *et al.* (2006) and not considered here). By gradually raising the frequency of the inlet forcing starting from a low value, the minimum frequency at which the flow synchronizes to the applied forcing defines the lower bound in frequency for 2D $\gamma_2$ waves. As the frequency is further increased, the waves become less and less isolated, the hump and capillary regions are less discernible as the ratio of the spatial extension of the hump and the length of capillary waves decreases. This behaviour is illustrated in figure 6, which presents time records of the film height at different forcing frequencies for $\beta = 10°$ and $Re = 34$. At $f = 3.6$ Hz, the waves are quasi-solitary with an extended capillary region. Increasing the frequency reduces the number of ripples and lowers the difference between the extension of the hump and the typical length of the capillary ripples. At higher frequencies, the primary wave train undergoes spatial modulations which generates a 2D sideband instability. Similar spatial modulations of multi-trough $\gamma_1$ wave trains have been reported by Liu & Gollub (1994). The onset of spatial modulations of the wave train determines the upper bound of the frequency.

The above procedure used to determine the domain of occurrence of 2D $\gamma_2$ waves has been repeated for $\beta$ in the range 5–18° with a step of 1°. We have then considered their domain of stability with respect to 3D perturbations. For a given couple of parameters $f$ and $\beta$, the Reynolds number is gradually raised until 3D wave trains are observed, which determines $Re_c^{3D}$.

The two types of 3D patterns, either rugged waves (figure 5b) or scallop waves (figure 5c), have been detected depending on the inclination angle. At small inclination angles, a short-wave mode is observed in the region of the capillary waves. At higher inclination angles, a long-wave mode is triggered and coexists on scallop waves with the short-wave mode (see figure 5c). For the two regions, $\Delta Re_c$ lies in the range 28–53 and increases with $f$.

### 4.3. *Capillary modes*

In this section, we focus on the short-wave instability mode of the 2D $\gamma_2$ waves. Figure 7(a) presents a typical topography of rugged waves obtained from the Schlieren acquisition technique. Parameters are $\beta = 8.3°$, $Re = 60$, $f = 3.5$ Hz, $\nu = 1.05 \times 10^{-6}$ m² s⁻¹, $\Gamma = 6013$ (depicted by a cross on figure 5a corresponding to $Re_c^{3D} = 49.7 \pm 0.9$). Three-dimensional modulations are restricted to the capillary region of the waves. The maximal deformation in the transverse direction $z$ is observed on the first capillary ripple, whose amplitude is also maximal. Instead, the front of the main wave is almost not affected by the presence of the 3D patterns, which implies that the wave speed in the 3D regime is very close to the 2D one. Noteworthy is the fact that successive modulations of the peaks (or troughs) of the capillary ripples exhibit a $\pi$ phase shift (see figure 7b).

We next question the ability of the linear stability analysis presented in § 2.4 to reproduce the experimental observations. Figure 7(c) displays a snapshot of the free-surface deformation obtained by superimposing the 2D $\gamma_2$ solution to the WRIBL model (2.3) with the eigenfunction corresponding to the maximum growth rate. The amplitude of the eigenmode has been adjusted so as to facilitate comparisons with the experimental results displayed in figure 7(b). Agreement between experimental and numerical snapshots prove to be very satisfactory. The short-wave mode characteristics are well captured by the most amplified eigenmode. In particular, the pronounced deformation of the capillary ripples, the observed checkerboard pattern (which results from the $\pi$ phase-shift between successive crests), the undeformed hump region, are qualitatively and quantitatively reproduced by the 3D linear stability analysis. Indeed, the experimental spanwise wavelength is 10 mm which is in good agreement with the result of the stability analysis (9.1 mm). This result indicates that the sidewall effects on the development of the capillary mode are negligible.

Finally, the energy budget of the linear perturbations offers an opportunity to identify the mechanism responsible for the destabilization of the capillary region. Following the procedure outlined in § 2.5, the most important contributions $\lambda_n$ to the kinetic energy budget (2.11) are presented in figure 8, along with the maximum growth rate (thick solid line), as functions of the transverse wavenumber $k_z$. Let us first note that $k_z = 0$ is at least a marginal mode thanks to the phase invariance of the 2D waves (Skotheim *et al.* 2003). In fact, for the set of parameters corresponding to figure 7, the maximum growth rate $\lambda$ at $k_z = 0$ is found to be positive, the $\gamma_2$ wave being unstable with respect to 2D perturbations. The 3D nature of the secondary instability results from the departure of the different contributions $\lambda_n$ of the kinetic energy budget from their values at the reference $k_z = 0$. In the name of convenience,
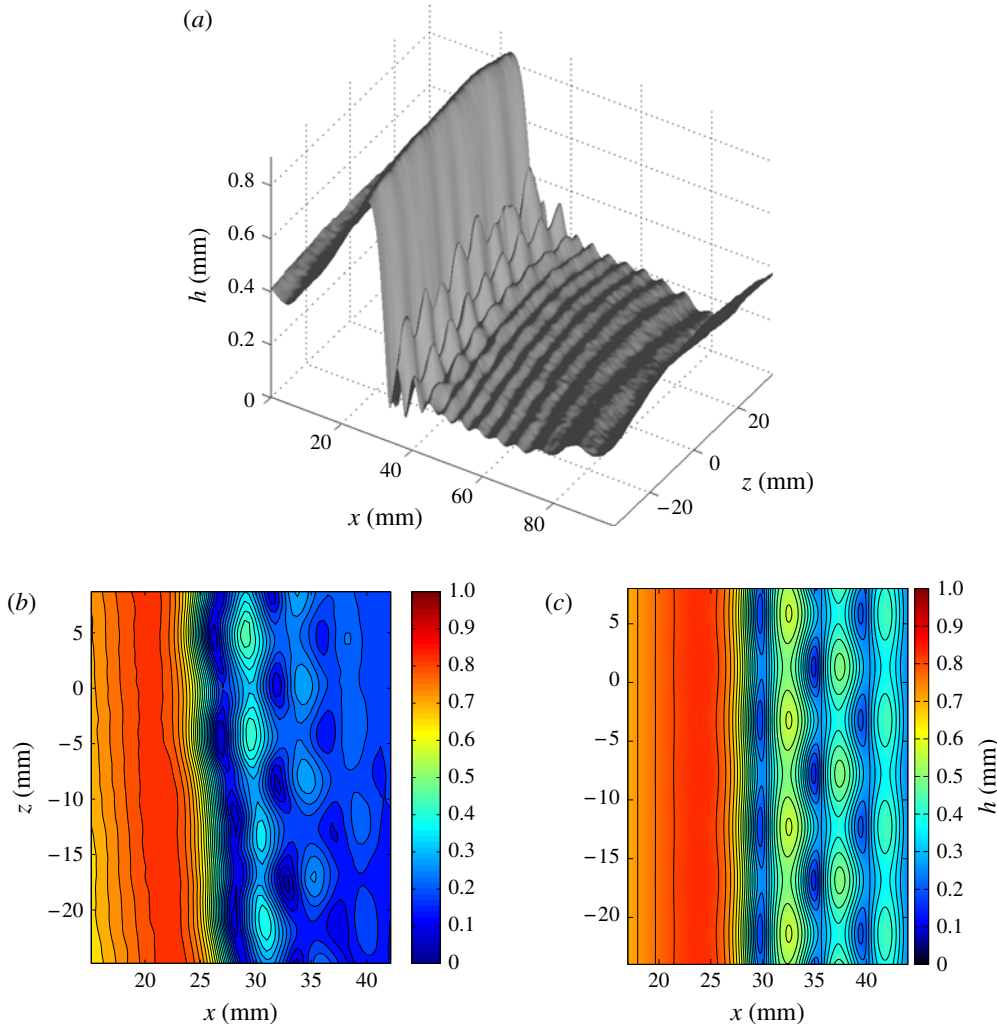
FIGURE 7. (Colour online) (*a*) 3D Schlieren topography for the case ($\beta = 8.3°$, $Re = 60$, $f = 3.5$ Hz, $\nu = 1.05 \times 10^{-6}$ m$^2$ s$^{-1}$, $\Gamma = 6013$) corresponding to the leftmost cross depicted in figure 5(*a*). 3D patterns of short wavelength are observed in the capillary region of a $\gamma_2$ solitary wave. (*b*) Experimental isothickness contours. (*c*) Superposition of the 3D numerical eigenfunction to the 2D base state.

contributions $\lambda_n$ are thus said to be stabilizing, that is to damp 3D perturbations, if their departure form the reference state $k_z = 0$ is negative. Conversely, contributions are said to be destabilizing if they promote 3D perturbations as compared with 2D ones, i.e. when their departure from the reference state $k_z = 0$ is positive. In what follows, without impediment to the clarity of the exposure, departures of $\lambda_n$ from their values at $k_z = 0$ are substituted to $\lambda_n$ themselves.

Our results presented in figure 8 indicate that surface tension contributions to the energy budget are all but one destabilizing. In addition, the most destabilizing one corresponds to the streamwise gradient of surface tension, i.e. $(5/6\delta)[h_0\tilde{h}'''\bar{\tilde{q}} + h_0'''\tilde{h}\bar{\tilde{q}}]$, referred to as '*q*-surface-tension *x*' terms. Noteworthy is the significant augmentation of this contribution for the most amplified perturbation at $k_z \approx 7$ cm$^{-1}$. Therefore, the
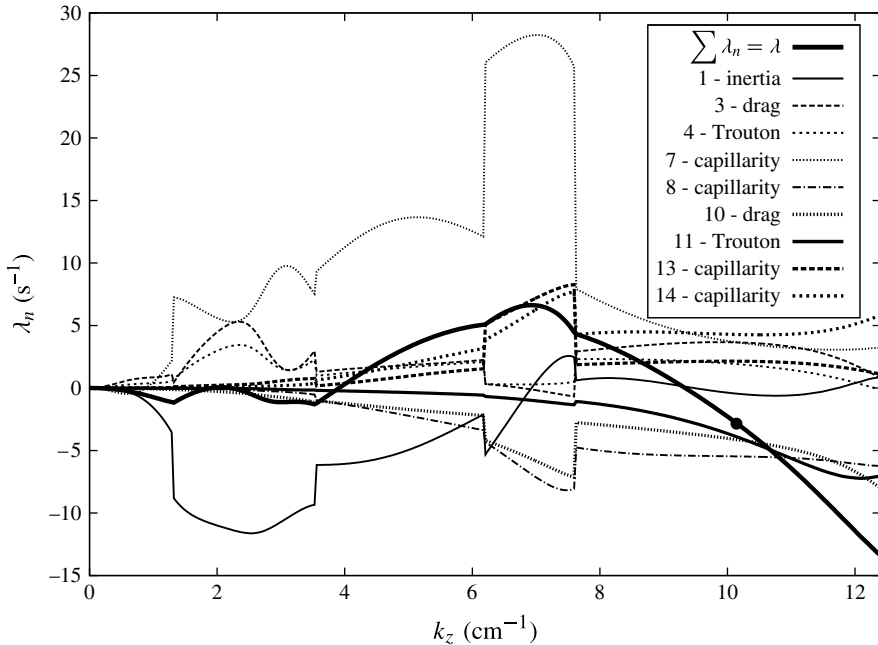
FIGURE 8. Energy budget issued from the stability analysis of the 2D $\gamma_2$ wave for the parameter set corresponding to figure 7. Contributions $\lambda_n$ are listed in table 2 in appendix B. For each contribution $\lambda_n$ as well as for the total, i.e. the growth rate $\lambda_r$, the reference value at $k_z = 0$ has been subtracted ($\lambda_r(k_z = 0) = 2.85 \text{ s}^{-1}$). The contributions which do not contribute to the 3D instability are not reported. The range of unstable wavenumber ($\lambda_r > 0$) extends from zero to $k_z \approx 10.1 \text{ cm}^{-1}$ (indicated by a solid circle).

short-wave 3D secondary instability of $\gamma_2$ waves emanates from the surface tension gradients in the capillary region of $\gamma_2$ waves. Because of its origin, this short-wave mode will be referred to as a capillary mode. Besides, the onset of this capillary mode being triggered by streamwise curvature of the ripples suggests a Rayleigh–Plateau mechanism. Each capillary ripple can be viewed as a succession of half cylinders with axes that are aligned with the $z$ axis, in which case the (stabilizing) axial curvature is $\propto \partial_{zz}h$ and the azimuthal (destabilizing) curvature is $\propto \partial_{xx}h$. The 3D short-wave instability offers a mechanism to reduce the free-surface area which tends to increase with the accumulation of capillary ripples at the front of solitary waves.

However, the analysis is more complex. As can be seen from figure 8, the contributions $\lambda_n$ are discontinuous functions of $k_z$. Each discontinuity signals the substitution of the most amplified eigenmode by another mode. Five successive changes of dominant eigenmodes are observed, which considerably complicates the analysis. Instead of a single capillary mode, two are found to be in competition. The transition between the most amplified modes strongly depends on the inclination angle. Figure 9(a) presents the growth rate of 3D perturbations as a function of $k_z$ for four different inclination angles, the other parameters being kept constant. For $\beta < 12°$, the most amplified eigenmode is the capillary mode identified in figure 8 and illustrated in figure 7. This mode is stationary. Instead, if $\beta$ exceeds $12°$, the most amplified capillary mode is oscillatory, characterized by two conjugate eigenvalues with eigenvectors corresponding to oblique waves propagating toward $z > 0$ and $z < 0$.
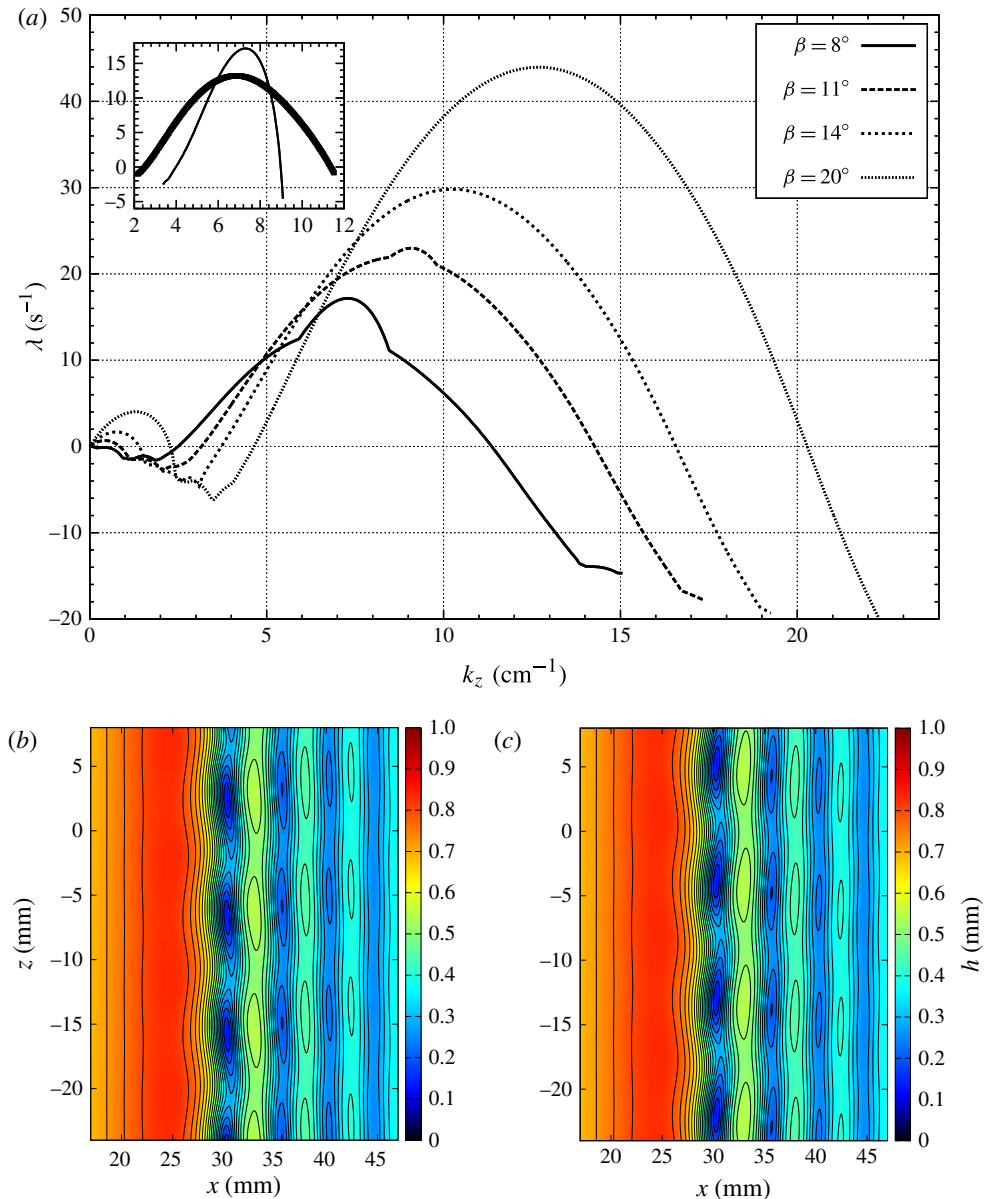
FIGURE 9. (Colour online) Competition between capillary modes as $\beta$ is varied. (*a*) Three-dimensional instability growth rate $\lambda$ as a function of the spanwise wavenumber $k_z$ for four values of $\beta$ ($Re = 50$, $\lambda_x = c/f = 45.7$ (non-dimensional), $\nu = 10^{-6}$ m$^2$ s$^{-1}$, $\sigma = 72$ mN m$^{-1}$). The inset is a close-up showing the two most unstable eigenvalues for $\beta = 8°$. (*b,c*) The free-surface pattern corresponding to the superposition of the 2D wave with the oscillatory mode.

The corresponding free-surface patterns are shown in figure 9(*b,c*). However, this oscillatory mode has not been observed in the experiments. Its occurrence coincides with the onset of the long-wave mode which is the subject of the next subsection.

In addition, sidewall effects break the invariance of the 2D wave in the transverse direction and therefore preclude the propagation of oblique waves (figure 3c).

## 4.4. *Inertial mode*

In this section, we consider the long-wave instability mode occurring when the plane is sufficiently inclined. Figure 10 presents experimental observations of scallop waves resulting from the long-wave instability. Parameters are $\beta = 17°$, $Re = 53$, $f = 5.1$ Hz, $\nu = 1.01 \times 10^{-6}$ m$^2$ s$^{-1}$, $\Gamma = 5024$ corresponding to the rightmost cross in figure 5(a) for which $Re_c^{3D} = 42.6 \pm 0.9$. Contrary to rugged waves promoted by the purely capillary mode (illustrated in figure 7), the whole wave, that is both the main hump and the capillary region, is modulated in the transverse direction. Modulations of different wavelengths, around 6 and 80 mm approximately, are discernible in the experimental wave pattern (figure 10b). The short-wave modulations are more pronounced in the capillary region, which supports the idea that the observed pattern originates from the combination of the capillary mode reported in the previous subsection, and of another long-wave mode. Floquet analysis based on the two-equation model (2.3) points to this conclusion. The growth rate of the most amplified transverse perturbations is drawn in figure 11 as a function of the transverse wavenumber $k_z$ (solid thick line). Two local maxima are observable corresponding to wavelengths of 5.8 and 67 mm, respectively, in good agreement with the experimental snapshots. Figure 10(c) presents a numerical reconstruction of the free surface pattern obtained from the combination of the 2D $\gamma_2$ solution to (2.3) and the two eigenmodes corresponding to the local maxima of the growth rate. This numerical reconstruction agrees well with the experimental snapshot (figure 10b) which provides further evidence for the involvement of the short-wave capillary mode with another long-wave mode. The energy budget (2.11) shed some light on the origin of the long-wave mode, which is found to be stationary (the imaginary part of the growth rate is zero). Indeed, the most destabilizing term in the long-wavelength region is the streamwise inertia in the streamwise momentum balance, whose rise and decline match with the location of a local maximum (see figure 11 and its insert). We thus conclude to the inertial nature of the long-wave 3D instability mode, and refer to it as the inertial mode.

## 5. Discussion

### 5.1. *Instability threshold*

Delineation of the experimental results has been made possible in terms of the competition between a capillary and an inertial instability mode. We now pay attention to the prevalence domains of these two instability modes in order to explain the change of regime observed in the stability chart presented in figure 5.

The reported short-wave instability mode has a capillary origin. However, the physical ingredient responsible for the existence of an instability threshold and thus the stabilization of the flow at low Reynolds number remains unclear. The localization of the instability eigenmode in the capillary region of the wave suggests that the onset of the instability is related to the amplitude of the capillary ripples, or perhaps more relevantly, to the amplitude of the curvature in this region of the wave. A simple argument based on the balance of the gradient of surface tension $\sim h \partial_{xxx} h$ and inertial terms $\sim \delta (q/h) \partial_x q$ gives $x = O(\delta^{-1/2})$ with $h = O(1)$ and $q = O(1)$ (Kalliadasis *et al.* 2012). The amplitude of the curvature in the capillary region of the solitary wave is
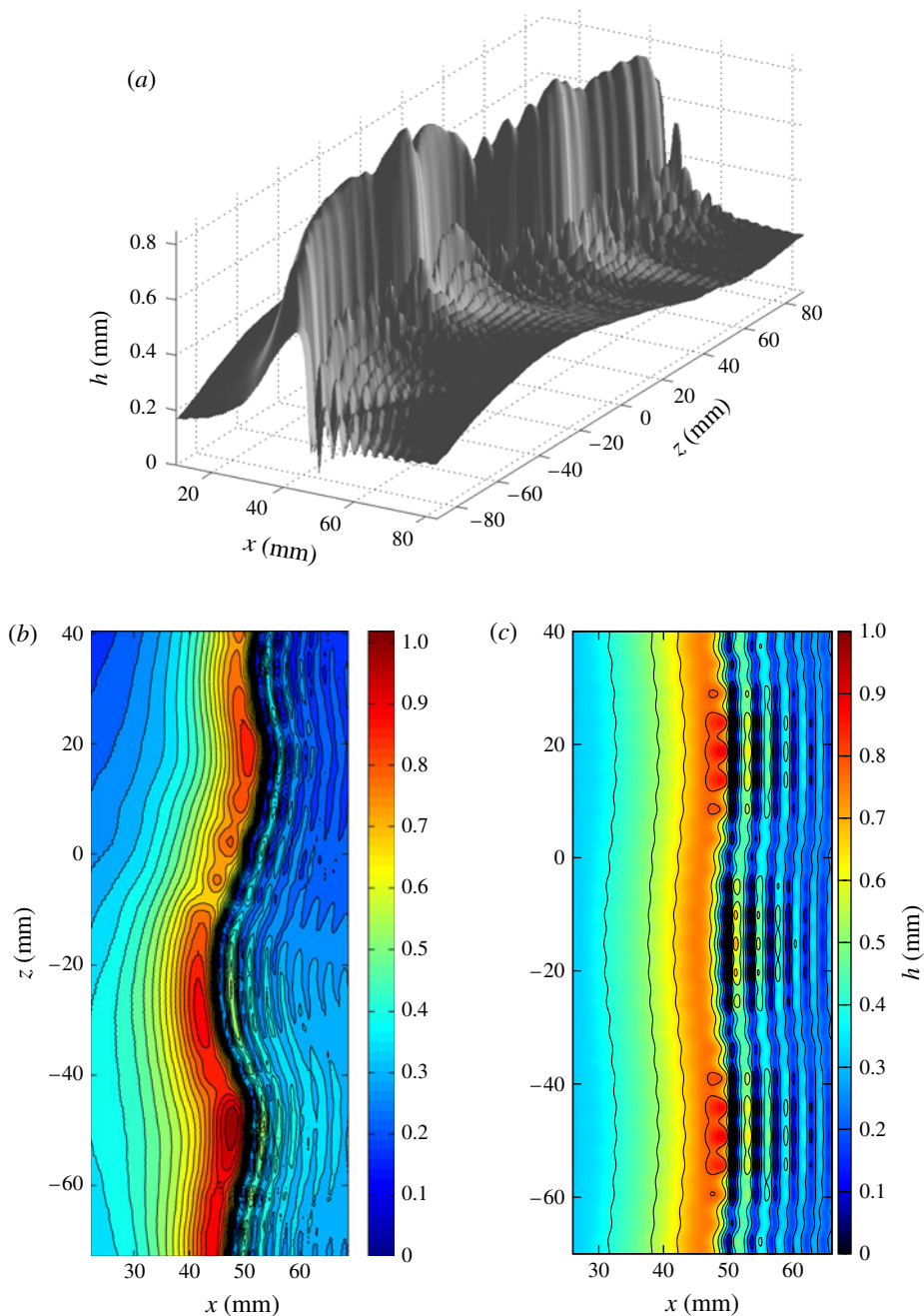
FIGURE 10. (Colour online) (*a*) Three-dimensional Schlieren topography ($\beta = 17°$, $Re = 53$, $f = 5.1$ Hz, $\nu = 1.01 \times 10^{-6}$ m$^2$ s$^{-1}$, $\Gamma = 5024$) corresponding to the rightmost cross depicted in figure 5(*a*). Competition between a short-wave and a long-wave instability mode. (*b*) Experimental isothickness contours. (*c*) Superposition of the 3D numerical eigenfunctions to the 2D base state.
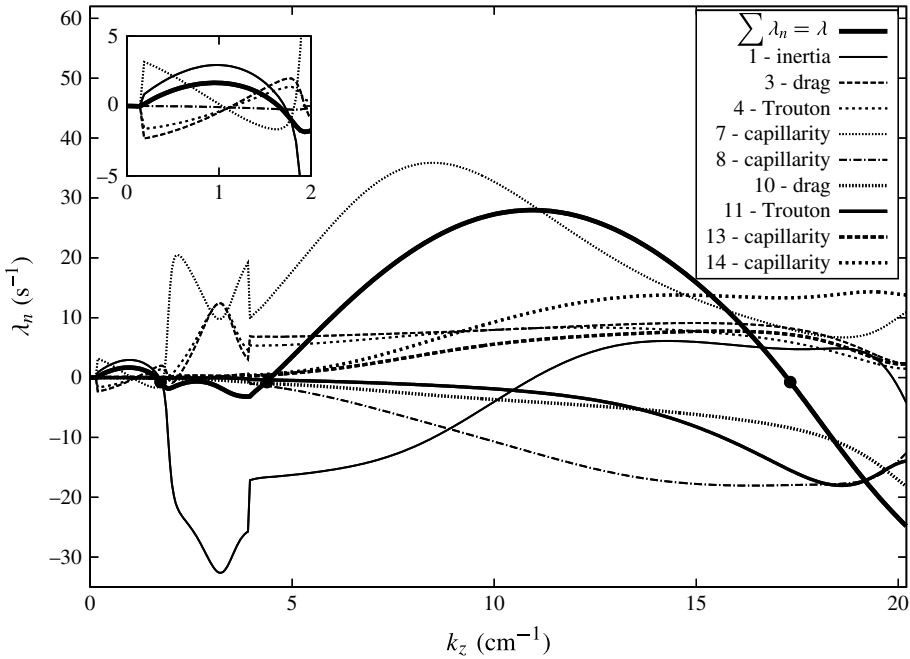
FIGURE 11. Energy budget issued from the stability analysis of the 2D $\gamma_2$ wave for the parameter set corresponding to figure 10($a$). Contributions $\lambda_n$ are listed in table 2 in appendix B. For each contribution $\lambda_n$ as well as for the total, i.e. the growth rate $\lambda_r$, the reference value at $k_z = 0$ has been subtracted ($\lambda_r(k_z=0)=0.76$ s$^{-1}$). The range of unstable wavenumbers extends from zero to $k_z \approx 17$ cm$^{-1}$ (indicated by a solid circle).

thus proportional to $\delta$. This suggests that the onset of the short-wave capillary mode corresponds to a certain threshold for the reduced Reynolds number, $\delta_c$ say. From (2.1) and (2.4), $\delta = \delta_c$ gives

$$Re_c^{3D} = \tfrac{1}{3}\delta_c^{9/11}\Gamma^{3/11} \propto (\sin\beta)^{-1/11}, \tag{5.1}$$

since $\Gamma \propto (\sin\beta)^{-1/3}$.

Turning to the long-wave mode, its inertial origin suggests an instability mechanism related to the local acceleration of the liquid–gas interface. Since Lord Rayleigh's pioneering work (Rayleigh 1883), a dense liquid overhanging a lighter one in a gravity field is known to be an unstable situation. More generally, an interface separating two fluids of different densities is unstable if the acceleration in the frame of reference moving with the interface is pointing towards the lighter fluid (Taylor 1950). As a consequence, a dense liquid underlying a lighter one can be unstable if the interface is accelerating downwards (in which case the relative acceleration in the frame of the interface is oriented upwards). This instability mechanism is involved, for instance, in the fingering instability of the liquid crown ejected by a drop splashing (Allen 1975), or in the azimuthal secondary instability of a sheared liquid jet (Marmottant & Villermaux 2004), and is proposed below as a possible premise for the long-wave inertial instability of $\gamma_2$ waves.

Let us consider a wave crest, sketched in figure 12, and focus on a point at the free interface in its local frame of reference $(X, Y)$. This point undergoes a relative
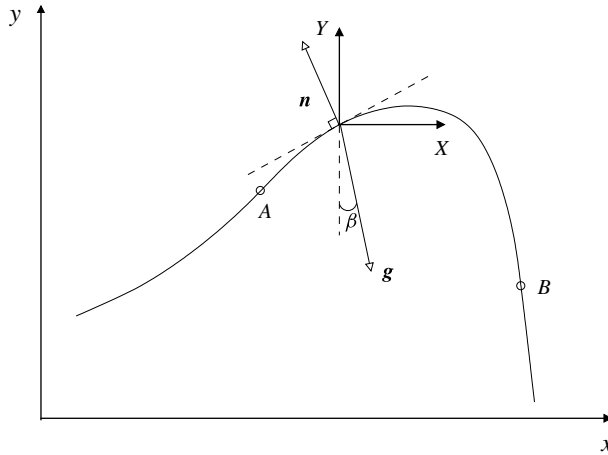
FIGURE 12. Sketch of a wave crest.

acceleration whose projection $a_r$ in the normal direction to the interface, written in dimensional form, is

$$a_r = \left( \boldsymbol{g} - \frac{\partial^2 h}{\partial t^2} \boldsymbol{e}_y \right) \cdot \boldsymbol{n}, \tag{5.2}$$

where $\boldsymbol{n}$ refers to the normal vector directed from the liquid to the gas. Considering a travelling wave moving at the speed $c$ and within the long-wave approximation, equation (5.2) reads

$$a_r = \left( \begin{array}{c} g \sin \beta \\ -g \cos \beta - c^2 \dfrac{\mathrm{d}^2 h}{\mathrm{d}\xi^2} \end{array} \right) \cdot \left( \begin{array}{c} -\dfrac{\mathrm{d}h}{\mathrm{d}\xi} \\ 1 \end{array} \right), \tag{5.3}$$

where $\xi = x - ct$ is the moving frame coordinate.

The interface remains stable if the relative acceleration points downwards ($a_r < 0$), which reads

$$c^2 \frac{\mathrm{d}^2 h}{\mathrm{d}\xi^2} + g \cos \beta + g \sin \beta \frac{\mathrm{d}h}{\mathrm{d}\xi} > 0. \tag{5.4}$$

For the solitary-like $\gamma_2$ waves considered in this study, the inertial long-wave mode is observed to develop at the crests of the waves. Therefore, the stability criterion (5.4) is expected to be first violated in regions surrounding the local maximum height ($\mathrm{d}^2 h/\mathrm{d}\xi^2 < 0$ and $\mathrm{d}h/\mathrm{d}\xi \approx 0$), materialized by the $A$ to $B$ segment in the sketch 12. As a consequence, $g \sin \beta \mathrm{d}h/\mathrm{d}\xi$ is expected to be negligible as compared with the other two terms in (5.4) at the onset of the long-wave inertial mode. Balancing $c^2 (\mathrm{d}^2 h/\mathrm{d}\xi^2) \sim U^2/L$ and $g \cos \beta$, where $U$ and $L$ stand for velocity and length scales, gives $U^2/(gL \cos \beta) = O(1)$. Selecting $U = g \sin \beta \bar{h}_N^2/(3\nu)$ and $L = \bar{h}_N$ corresponding to the Nusselt solution defines a critical Froude number $Fr_c$ above which the instability sets in, or equivalently

$$Re_c^{\mathrm{3D}} = \tfrac{1}{3} Fr_c^2 \cot \beta \propto \cot \beta. \tag{5.5}$$

Equation (5.5) must be contrasted with (5.1). *A priori*, the thresholds $\delta_c$ and $Fr_c$ are not constants but depend on the shape of the $\gamma_2$ wave and are functions of
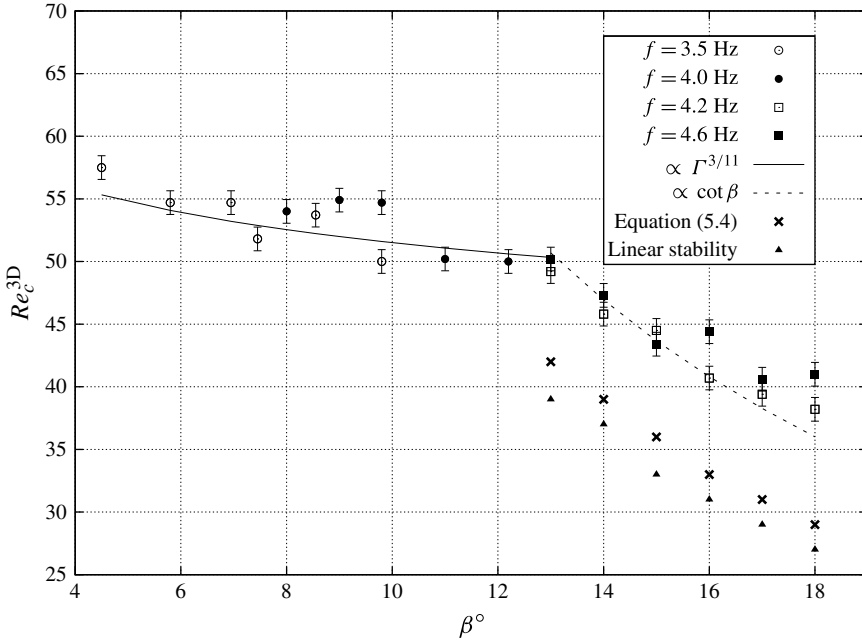
FIGURE 13. Three-dimensional instability threshold $Re_c^{3D}$ as function of the inclination angle $\beta$ for different values of $f$. Lines correspond to the predictions (5.5) and (5.1) ($\nu = 1.08 \times 10^{-6}$ m$^2$ s$^{-1}$). Numerical thresholds from the criterion (5.4) and Floquet stability analysis are indicated.

the forcing frequency $f$. Yet, this dependence on $f$ is expected to be weak if the waves are sufficiently isolated at sufficiently low frequencies. Formulae (5.5) and (5.1) are put to the test against experimental evidence in figure 13. Critical Reynolds number $Re_c^{3D}$ is plotted versus the inclination angle $\beta$ for forcing frequencies in the range [3.5, 4.6] Hz. This choice enables us to cover a reasonably large interval of inclination angle, which otherwise is quite limited for a single frequency due to the limitations of the experimental procedure outlined in §4.2, and warrants that the waves are sufficiently isolated. Experimental data are observed to form two clusters of points that are satisfactorily fitted by (5.5) and (5.1) with $\delta_c \approx 26$ and $Fr_c^2 \approx 6$. The intersection between the two curves occurs at $\beta \approx 13°$ which roughly corresponds to the transition between rugged and scallop waves observed in our experiments.

The Floquet stability analysis based on the two-equation model (2.3) provides another tool to validate the predictions (5.5) and (5.1). Figure 13 has been completed with the numerical results from the Floquet theory for the $\gamma_2$-wave solutions to (2.3) at a frequency $f = 4.2$ Hz. Agreement with (5.5) is convincing, although the threshold $Fr_c$ differs from the experimental data, as numerical thresholds are significantly lower than the experimental ones. This discrepancy may have several origins. One possible explanation is the fixed location of the recorded experimental data, $x \sim 30$ cm. Perturbations that are not sufficiently amplified may remain undetected at that location, which suggests that experimental thresholds must be higher than numerical ones in agreement with our findings. Another reason for this discrepancy lies in the simplifications leading to the simplified model (2.3) with respect to the basic set of equations.

Finally, the onset of a Rayleigh–Taylor instability has been looked after by monitoring the stability criterion (5.4) for the solutions to (2.3). A remarkable agreement is achieved with the Floquet stability analysis although the Rayleigh–Taylor criterion (5.4) slightly underestimates the instability threshold. However, the wavelength and spatial growth rate values calculated by this method are higher than expected which may be due, as was pointed by Krechetnikov (2009), to the surface curvature. As a whole, we can however conclude that the proposed Rayleigh–Taylor mechanism for the onset of the long-wave instability mode is supported by numerical and experimental evidence.

### 5.2. *Influence of the liquid viscosity and surface tension on the 3D instability*

We end this section by considering the influence of the liquid properties on the secondary 3D instability of the quasi-solitary $\gamma_2$ waves. The analysis presented here is principally based on the numerical results from the Floquet theory.

We first consider the influence of the viscosity. Figure 14 presents the growth rate of the most amplified perturbation as function of the transverse wavenumber $k_z$ as obtained from our Floquet analysis. Inclination angle and Reynolds number are set to $\beta = 20°$ and $Re = 50$ so that both capillary and inertial modes are excited. The dimensionless longitudinal wavelength $\lambda_x = 45$ is kept constant, which guarantees that the $\gamma_2$ wave remains quasi-solitary. Kinematic viscosity is varied in the range $\nu \in [1, 6] \times 10^{-6}$ m$^2$ s$^{-1}$, corresponding to typical water–glycerine mixture ($\Gamma \in [390, 4806]$). A significant damping of the capillary mode is observed as viscosity is raised. The local maximum of the growth rate corresponding to the capillary mode decreases with viscosity and is reached at larger values of the dimensionless transverse wavenumber $k_z$ (figure 14$a$). These effects on the capillary mode are consequences of the attenuation of the capillary ripples by the Trouton elongational viscosity. The viscous dispersion parameter $\eta$ being augmented from 0.033 to 0.16, the profile of the wave is considerably modified as can be observed from the two insets in figure 14($a$). Number and amplitude of the capillary ripples dwindle as $\eta$ increases. Ripples also present a shorter dimensionless wavelength. These alterations of the wave profile are consistent with the reported effects on the capillary mode of secondary instability. Instead, the inertial mode is almost unaffected by the variations of the viscosity, as a small decrease of the local maximum of the growth rate at $k_z \approx 0.3$ is noticeable. Indeed, the amplitude and shape of the hump region of the waves are only weakly altered, which explains that the Rayleigh–Taylor instability mechanism remains strong.

When recast using original dimensional quantities (see figure 14$b$), the growth rate of the most amplified perturbations presents however a local maximum for the capillary mode at a wavenumber $k_z$ which actually decreases with the viscosity. This is a consequence of the variation of the length scale $\kappa \bar{h}_N$ of the wave from 2 mm at $\nu = 10^{-6}$ m$^2$ s$^{-1}$ to 2.9 mm at $\nu = 6 \times 10^{-6}$ m$^2$ s$^{-1}$, the Nusselt film thickness $\bar{h}_N \propto \nu^{2/3}$ being an increasing function of the viscosity at constant Reynolds number ($\kappa \propto \nu^{-4/9}$ which gives $\kappa \bar{h}_N \propto \nu^{2/9}$). For the same reason, the wavenumber corresponding to the local maximum of the growth rate for the inertial mode is also a decreasing function of viscosity.

The influence of the surface tension is discussed in figure 15. Here $\sigma$ is decreased from 72 to 15 mN m$^{-1}$. The Kapitza number $\Gamma$ thus decreases from 4806 to 962. The evolutions of the local maxima of the dimensionless growth rate corresponding to the capillary and inertial modes are similar to what is observed when the viscosity is raised. The inertial mode remains unaffected. Attenuation of the capillary mode
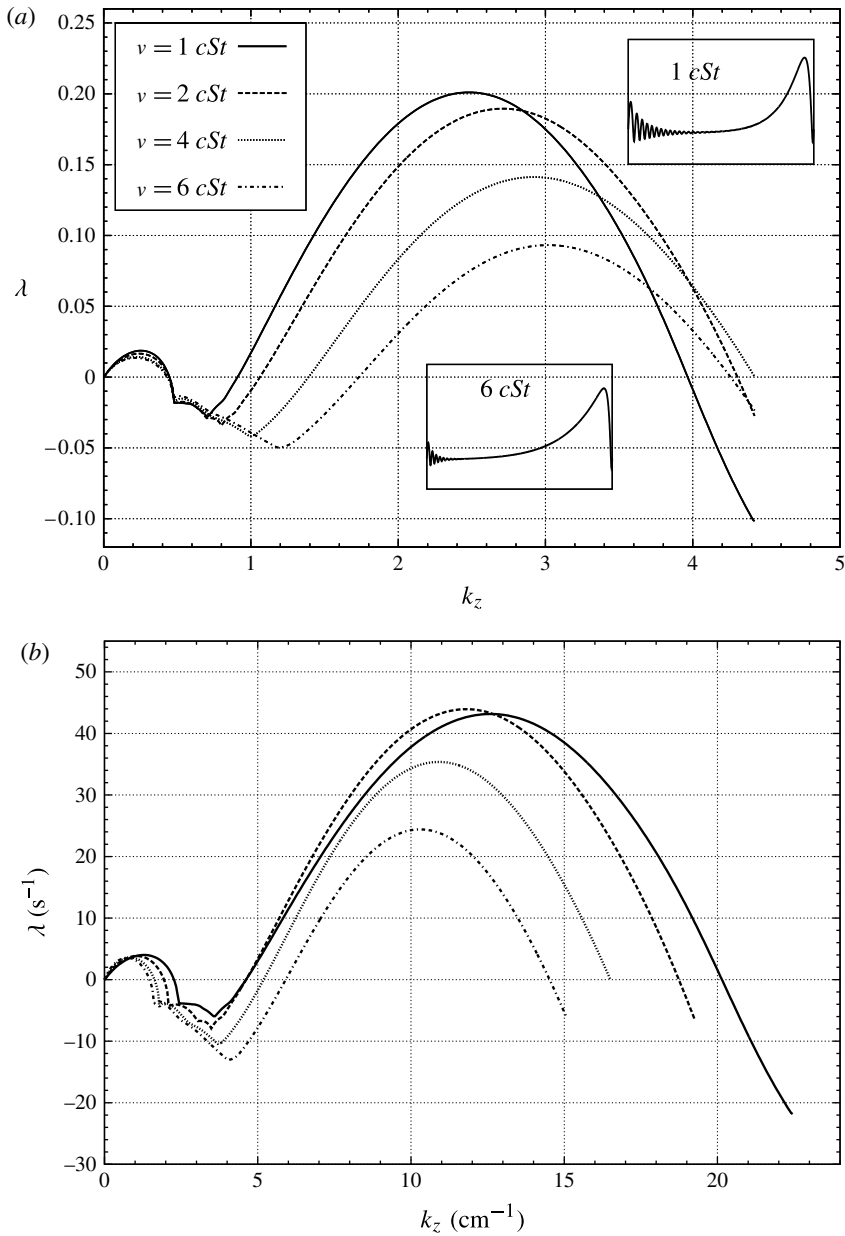
FIGURE 14. Influence of the liquid viscosity on the 3D linear stability of $\gamma_2$ quasi-solitary waves. The maximum growth rate $\lambda$ is shown versus the transverse wavenumber $k_z$. Parameters are: $\beta = 20°$, $\lambda_x = 45$ (in non-dimensional units), $Re = 50$, $\sigma = 72$ mN m$^{-1}$. (*a,b*) Non-dimensional and dimensional quantities respectively. The streamwise wavelength and celerity for the wave profiles shown in insets are $\lambda_x = 8.9$ cm, $c = 40.9$ cm s$^{-1}$, $\Gamma = 4806$ ($\nu = 10^{-6}$ m$^2$ s$^{-1}$) and $\lambda_x = 13.2$ cm, $c = 62.6$ cm s$^{-1}$, $\Gamma = 390$ ($\nu = 6 \times 10^{-6}$ m$^2$ s$^{-1}$).
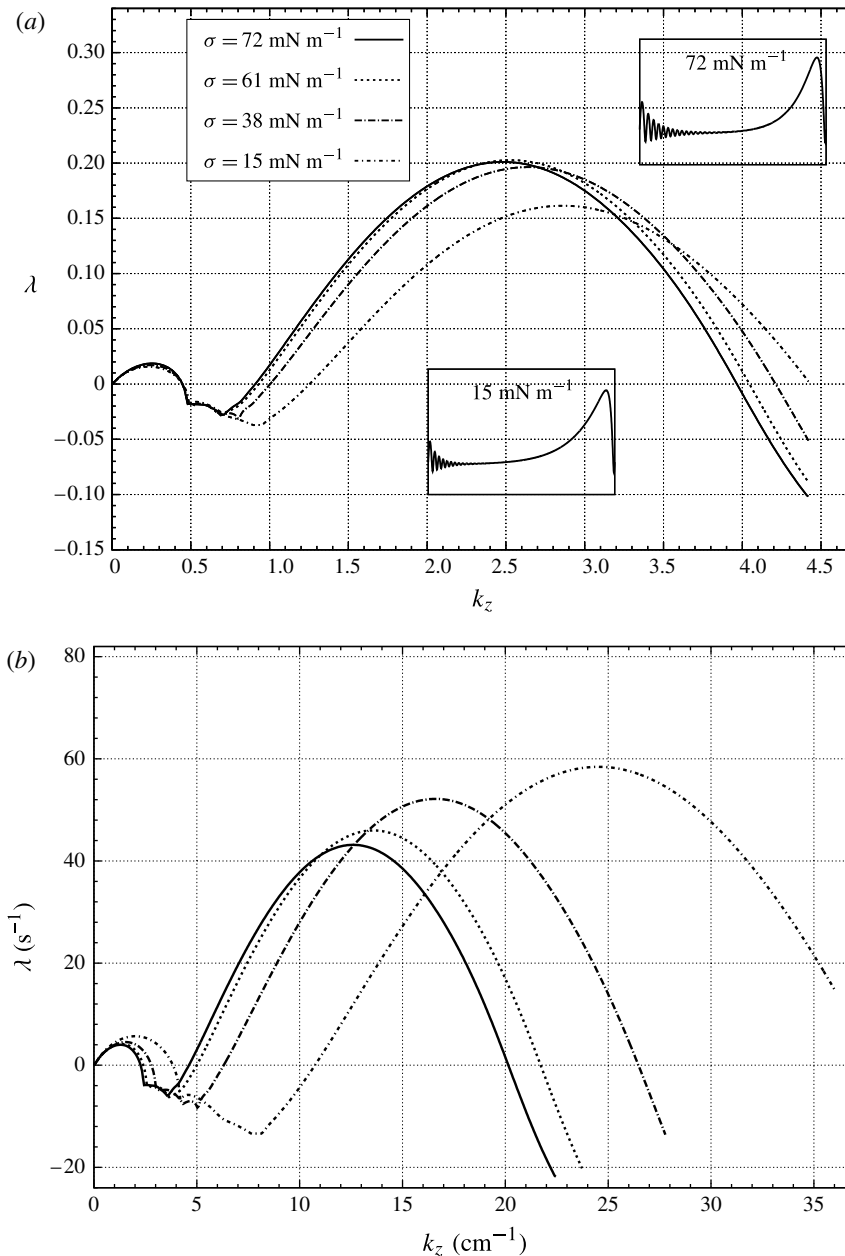
FIGURE 15. Influence of the liquid surface tension on the 3D linear stability results. Here $\nu = 10^{-6}$ m$^2$ s$^{-1}$. See the caption of figure 14 for the other parameters. The streamwise wavelength and celerity for the wave profiles shown in insets are $\lambda_x = 8.9$ cm, $c = 40.9$ cm s$^{-1}$, $\Gamma = 4806$ ($\sigma = 72$ mN m$^{-1}$) and $\lambda_x = 5.3$ cm, $c = 36.6$ cm s$^{-1}$, $\Gamma = 962$ ($\sigma = 15$ mN m$^{-1}$).

results from the enhancement of Trouton elongational viscosity which follows from the reduction of the Kapitza number (and thus the augmentation of the dispersion parameter $\eta$). Comparison of figures 14(*a*) and 15(*a*) suggests that the stability of the

waves is less affected by the variation of the surface tension than by the variation of the viscosity. Indeed, the Kapitza number varies in a range that is larger in figure 14($a$) than in figure 15($a$) since $\Gamma \propto \sigma / \nu^{4/3}$ and physically relevant viscosities cover a wider interval than surface tensions. However, when recast using dimensional quantities, the influence of the surface tension on the stability analysis is significantly different from what is observed with viscosity (compare figures 15$b$ and 14$b$). This difference is a direct consequence of the decrease of the length and time scales, $\kappa \bar{h}_N$ and $\kappa \nu / (g \bar{h}_N \sin \beta)$, as the capillary length $l_c$ reduces along with the surface tension.

We have next investigated the influence of Trouton elongational viscosity on the stability of $\gamma_2$ waves by varying $\eta = 1/\kappa^2$, while maintaining constant the two other reduced parameters, $\delta$, and $\zeta$ (results not shown). The amplitude and the speed of solitary waves depend mainly on the reduced Reynolds number $\delta$ whereas $\eta$ affects the amplitude of the capillary ripples. Raising $\eta$ by a factor five has been found to suppress the capillary mode while affecting the inertial mode only weakly, which is consistent with the previous discussions.

A thorough experimental study of the influence of viscosity and surface tension on the 3D stability is beyond the scope of the present paper. However, we end this section by presenting some experimental observations which support the above conclusions. Figure 16 presents three snapshots of modulated quasi-solitary waves at conditions that are close to those discussed in figures 14 and 15 ($\beta = 17.9°$ and $Re = 70$), for water, a 22 % per weight water–glycerin mixture and a 1.3 % per weight water–butanol solution. The water–glycerin mixture is twice as viscous as water with a surface tension that remains close to the value for water, whereas the water–butanol solution has a significantly lower surface tension than water but keeps a roughly equal viscosity. Figure 16($a$) is typical of modulated scallop waves on water films arising from the interplay of the capillary and inertial 3D instability modes. Short- and long-wave modes have wavelengths that can be estimated to be around 0.5 and 3.9 cm, respectively ($k_z = 12.6$ cm$^{-1}$ and 1.6 cm$^{-1}$) in good agreement with the predictions from the Floquet analysis presented in figures 14($b$) and 15($b$). Turning to the water–glycerin mixture (cf. figure 16$b$), the capillary region of the 2D waves is significantly damped and the capillary short-wave instability is not visible as an effect of the increment of viscosity. The long-wave inertial modulations of the crests remain unaffected however. Lowering surface tension instead (figure 16$c$) has a different effect. Although the capillary regions of the waves are not significantly damped, the Kapitza number remaining quite high, short-wave transverse modulations are not detected. Instead, the long-wave modulations are efficiently enhanced and the inertial mode supersedes the short-wave ones, which explains the disappearance of the corresponding modulations. We note that the latter amplification of the scallop waves cannot be anticipated from the above Floquet analysis, which is restricted to small-amplitude perturbations.

## 6. Summary–conclusion

In this paper, we have considered the stability of $\gamma_2$ travelling waves at the surface of a film flow down an inclined plane. These waves are fast, one-humped and quasi-solitary. They present a typical shape which can easily be decomposed into a hump region and a capillary region. Slow $\gamma_1$ waves, multi-humped waves, or waves whose shape cannot be decomposed into capillary and hump regions have been the subject of earlier studies (Liu *et al.* 1995; Scheid *et al.* 2006) and therefore have not been investigated here. The investigation is experimental and numerical using the
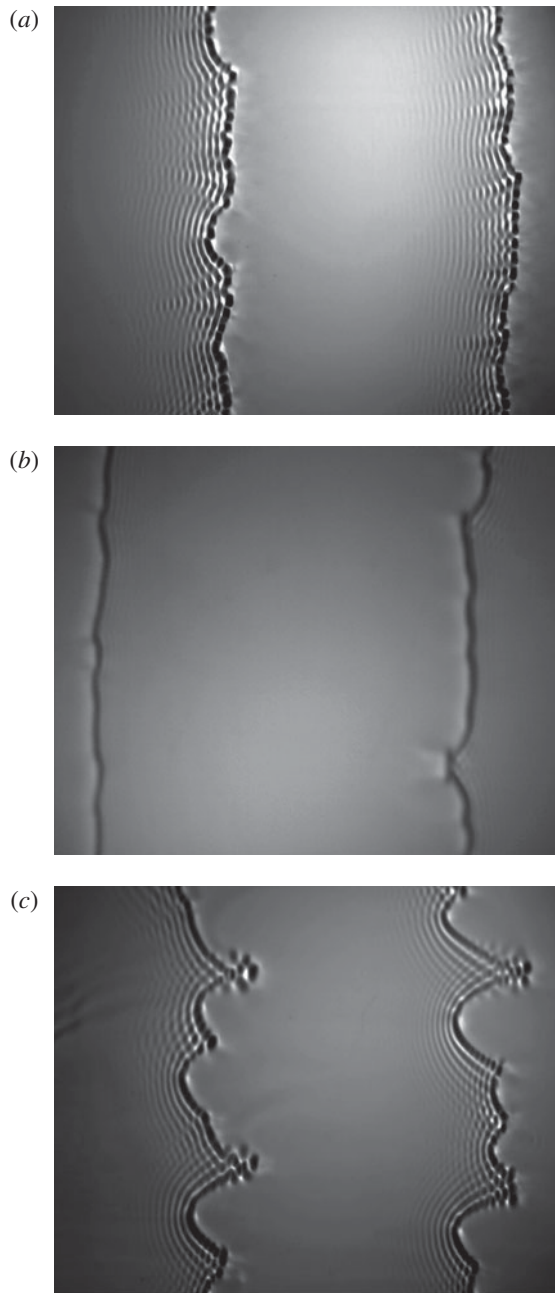
(*a*)

(*b*)

(*c*)



FIGURE 16. Experimental snapshots illustrating the influence of liquid viscosity and surface tension on the 3D patterns. Parameters are: $\beta = 17.9°$, $Re = 70$. (*a*) Water: $f = 4.5$ Hz, $\nu = 10^{-6}$ m$^2$ s$^{-1}$, $\sigma = 72$ mN m$^{-1}$, $\Gamma = 4806$. $\lambda_x = 9.4$ cm ($\lambda_x = 44$ in dimensionless units). (*b*) Water–glycerin mixture, 22 % per weight: $f = 4.9$ Hz, $\nu = 1.9 \times 10^{-6}$ m$^2$ s$^{-1}$, $\sigma = 70.6$ mN m$^{-1}$, $\Gamma = 1971$. $\lambda_x = 11.7$ cm ($\lambda_x = 48.4$ in dimensionless units). (*c*) Water–butanol solution, 1.3 % per weight: $f = 4.5$ Hz, $\nu = 1.1 \times 10^{-6}$ m$^2$ s$^{-1}$, $\sigma = 49$ mN m$^{-1}$, $\Gamma = 3000$. Here $\lambda_x = 9.1$ cm ($\lambda_x = 46.8$ in dimensionless units).

tools of Floquet stability analysis based on the solutions to a two-equation model (2.3) which has been abundantly validated with respect to experiments and direct numerical simulations elsewhere (Ruyer-Quil & Manneville 2000; Scheid *et al.* 2006).

A Schlieren technique, recently proposed by Moisy *et al.* (2009), has been implemented successfully providing accurate snapshots of the free surface on an extended area. This acquisition technique has been validated by means of comparisons with CCI measurements. High temporal ($>100$ Hz) and spatial (0.5 mm) resolutions are achieved providing 3D snapshots of the free surface over large domains (20 cm $\times$ 25 cm) with a precision of approximately 20 µm. Two-dimensional wave trains have been generated as the response of the flow to a periodic forcing at inlet. They undergo a 3D secondary instability if the flow rate (or Reynolds number) is sufficiently high. Two different wave patterns are then reported, either rugged waves or scallop waves. The prevalence of either pattern is influenced by the forcing frequency at inlet and the inclination angle. Rugged waves have been shown to be promoted by a short-wave transverse instability of capillary origin, whereas scallop waves emerge from a long-wave transverse instability prompted by inertial effects. Capillary short-wave instability predominates at small inclination angle, whereas the long-wave inertial instability is observed at larger inclination. The two instability modes are well captured by a secondary stability analysis based on (2.3). An energy budget of the perturbations has proved instrumental for the identification of the physical origin of the instabilities. The short-wave mode arises in the capillary region of the wave, with a mechanism of capillary origin which is similar to the Rayleigh–Plateau instability, the onset of 3D patterns enabling to reduce the contact area of the gas–liquid interface. Such a mechanism has been postulated by Demekhin & Kalaidin (2007), and erroneously associated with the long-wave instability mode. The latter mode is triggered by a Rayleigh–Taylor instability of a decelerated liquid interface. The threshold of the short-wave mode obeys $Re_c^{3D} \propto \Gamma^{3/11} \propto (\sin\beta)^{-1/11}$, whereas the onset of the long-wave mode rather verifies $Re_c^{3D} \propto \cot\beta$. Rugged waves are thus observed at relatively small inclination angles, the short-wave mode being excited before the long-wave one sets in. At larger angles, the long-wave mode predominates and scallop waves are observed. For water film and at sufficiently low forcing frequencies $f$, the transition between rugged and scallop waves is only weakly affected by $f$ and occurs around $\beta = 13°$ which corresponds to the intersection of the instability thresholds for the two inertial and capillary modes (cf. figure 13). This value of $\beta$ is certainly not universal. The occurrence and prevalence of rugged and scallop waves as surface tension and viscosity are varied require a thorough study that is beyond the scope of the present work and will be presented elsewhere. Transition from rugged to scallop waves coincides with a change of nature of the short-wave capillary mode from stationary to oscillatory. However, short-wave capillary modulations of scallop waves seem frozen and remain in-phase with the long-wave deformations of the fronts. We note that both the sidewall effects and the long-wave inertial mode break the translational invariance in the transverse $z$ direction that is necessary for the growth of an oscillatory mode.

To the best of the authors' knowledge, the onset of rugged waves related to a short-wave instability mode has not been reported previously, earlier studies being devoted either to the vertical geometry (Park & Nosoko 2003) or to more viscous fluids (Liu *et al.* 1995). Promoting rugged waves could be of interest in applications as 2D solitary waves travel faster and with a larger amplitude than 3D solutions (Demekhin *et al.* 2007). Similarly, an enhancement of backflow phenomena and flow separation in these waves might be expected, with interesting consequences on heat and mass transfer (Dietze *et al.* 2009).

| $n$ | Origin | Expression |
|---|---|---|
| 1 | $q$-inertia $x$ | $c\tilde{q}'\bar{\tilde{q}} - \dfrac{17}{7}\left[\dfrac{q_0}{h_0}\tilde{q}'\bar{\tilde{q}} + \dfrac{q_0'}{h_0}|\tilde{q}|^2 - \dfrac{q_0 q_0'}{h_0^2}\tilde{h}\bar{\tilde{q}}\right]$ $+ \dfrac{9}{7}\left[\dfrac{q_0^2}{h_0^2}\tilde{h}'\bar{\tilde{q}} - \dfrac{2h_0' q_0^2}{h_0^3}\tilde{h}\bar{\tilde{q}} + \dfrac{2q_0 h_0'}{h_0^2}|\tilde{q}|^2\right]$ |
| 2 | $q$-inertia $z$ | $-\dfrac{8}{7}\dfrac{q_0}{h_0}\mathrm{i}k_z\tilde{p}\bar{\tilde{q}}$ |
| 3 | $q$-viscous drag | $-\dfrac{5}{2\delta}\left[\dfrac{|\tilde{q}|^2}{h_0^2} - \dfrac{2q_0}{h_0^3}\tilde{h}\bar{\tilde{q}}\right]$ |
| 4 | $q$-'Trouton' viscosity | $\dfrac{4\eta}{\delta}\left[\dfrac{(h_0')^2}{h_0^2}|\tilde{q}|^2 - \dfrac{2q_0(h_0')^2}{h_0^3}\tilde{h}\bar{\tilde{q}} + \dfrac{2q_0 h_0'}{h_0^2}\tilde{h}'\bar{\tilde{q}}\right]$ $- \dfrac{9\eta}{2\delta}\left[\dfrac{h_0'}{h_0}\tilde{q}'\bar{\tilde{q}} + \dfrac{q_0'}{h_0}\tilde{h}'\bar{\tilde{q}} - \dfrac{q_0' h_0'}{h_0^2}\tilde{h}\bar{\tilde{q}}\right]$ $- \dfrac{6\eta}{\delta}\left[\dfrac{h_0''}{h_0}|\tilde{q}|^2 + \dfrac{q_0}{h_0}\tilde{h}''\bar{\tilde{q}} - \dfrac{q_0 h_0''}{h_0^2}\tilde{h}\bar{\tilde{q}}\right]$ $+ \dfrac{\eta}{\delta}\left[\dfrac{9}{2}\tilde{q}''\bar{\tilde{q}} - \dfrac{13}{16}\dfrac{h_0' k_z}{h_0}\mathrm{i}\tilde{p}\bar{\tilde{q}} + \dfrac{23}{16}\dfrac{q_0 k_z^2}{h_0}\tilde{h}\bar{\tilde{q}}\right]$ $+ \dfrac{\eta}{\delta}\left[-k_z^2|\tilde{q}|^2 + \dfrac{7}{2}k_z\mathrm{i}\tilde{p}'\bar{\tilde{q}}\right]$ |
| 5 | $q$-gravity | $\dfrac{5}{6\delta}\tilde{h}\bar{\tilde{q}}$ |
| 6 | $q$-hydrostatic pressure | $-\dfrac{5}{6}\dfrac{\zeta}{\delta}\left[h_0\tilde{h}'\bar{\tilde{q}} + h_0'\tilde{h}\bar{\tilde{q}}\right]$ |
| 7 | $q$-surface tension $x$ | $\dfrac{5}{6\delta}\left[h_0\tilde{h}'''\bar{\tilde{q}} + h_0'''\tilde{h}\bar{\tilde{q}}\right]$ |
| 8 | $q$-surface tension $z$ | $-\dfrac{5}{6}\dfrac{k_z^2}{\delta}h_0\tilde{h}'\bar{\tilde{q}}$ |
| 9 | $p$-inertia $z$ | $c\tilde{p}'\bar{\tilde{p}} - \dfrac{8}{7}\dfrac{q_0'}{h_0}|\tilde{p}|^2 - \dfrac{9}{7}\left[\dfrac{q_0}{h_0}\tilde{p}'\bar{\tilde{p}} - \dfrac{q_0 h_0'}{h_0^2}|\tilde{p}|^2\right]$ |
| 10 | $p$-viscous drag | $-\dfrac{5}{2\delta}\dfrac{|\tilde{p}|^2}{h_0^2}$ |
| 11 | $p$-'Trouton' viscosity | $\dfrac{\eta}{\delta}\left[-\dfrac{9}{2}k_z^2|\tilde{p}|^2 + \dfrac{13}{4}\dfrac{q_0 h_0'}{h_0^2}k_z\mathrm{i}\tilde{h}\bar{\tilde{p}} - \dfrac{h_0'}{h_0}\tilde{p}'\bar{\tilde{p}}\right]$ $+ \dfrac{\eta}{\delta}\left[-\dfrac{43}{16}\dfrac{h_0'}{h_0}k_z\mathrm{i}\tilde{q}\bar{\tilde{p}} - \dfrac{13}{16}\dfrac{q_0'}{h_0}k_z\mathrm{i}\tilde{h}\bar{\tilde{p}} + \dfrac{3}{4}\dfrac{(h_0')^2}{h_0^2}|\tilde{p}|^2\right]$ $+ \dfrac{\eta}{\delta}\left[-\dfrac{23}{16}\dfrac{h_0''}{h_0}|\tilde{p}|^2 - \dfrac{73}{16}\dfrac{q_0}{h_0}k_z\mathrm{i}\tilde{h}'\bar{\tilde{p}} + \tilde{p}''\bar{\tilde{p}} + \dfrac{7}{2}k_z\mathrm{i}\tilde{q}'\bar{\tilde{p}}\right]$ |
| 12 | $p$-hydrostatic pressure | $-\dfrac{5}{6}\dfrac{\zeta k_z}{\delta}h_0\mathrm{i}\tilde{h}\bar{\tilde{p}}$ |
| 13 | $p$-surface tension $x$ | $\dfrac{5}{6\delta}h_0 k_z\mathrm{i}\tilde{h}''\bar{\tilde{p}}$ |
| 14 | $p$-surface tension $z$ | $-\dfrac{5}{6\delta}h_0 k_z^3\mathrm{i}\tilde{h}\bar{\tilde{p}}$ |

TABLE 2. List of the $\lambda_n$ terms involved in the right-hand side of (2.11) before integration on a wavelength and division by $\langle\tilde{q},\tilde{q}\rangle$.
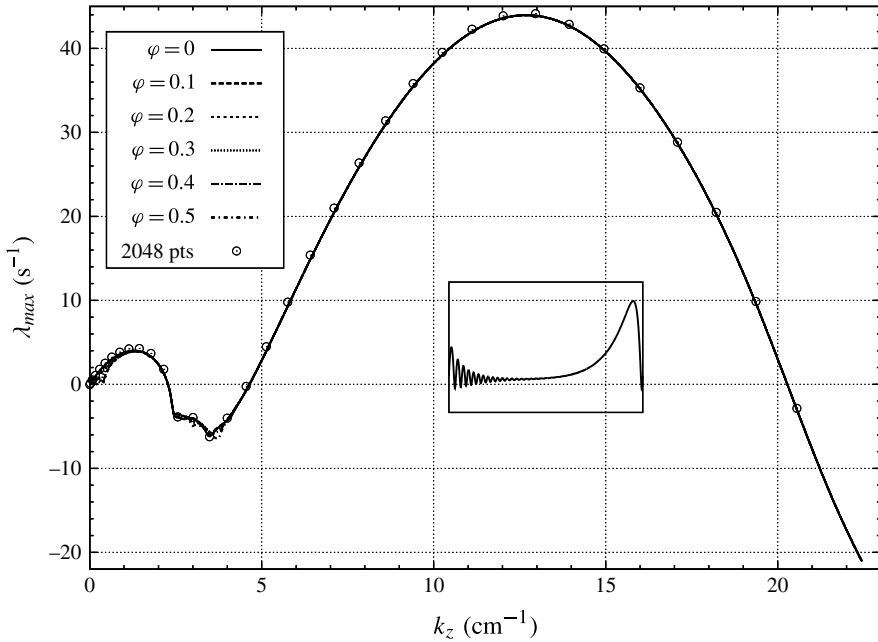
FIGURE 17. Maximum growth rate $\lambda_{max}$ as a function of the transverse wavenumber $k_z$ for different values of the detuning parameter $\varphi$ ($\beta = 20°$, $Re = 50$, $f = 4.6$ Hz, $\nu = 10^{-6}$ m$^2$ s$^{-1}$, $\sigma/\rho = 7.21 \times 10^{-5}$). Dots refer to the results obtained on a finer grid ($N = 2048$ nodes instead of $N = 1024$).

### Acknowledgements

### Appendix A. Floquet analysis: numerical procedure and influence of the detuning parameter

In this appendix we briefly discuss the numerical procedure that has been implemented to solve the linear differential eigenvalue problem (2.5). Details can be found in Ruyer-Quil (1999) and Kalliadasis *et al.* (2012). The base state $X_0$ and perturbation amplitude $\tilde{X}$ are discretized on a regular mesh of $N$ nodes. Their discrete representations $X_0^N$ and $\tilde{X}^N$ are vectors of dimension $3N$ that are converted in Fourier series of coefficients $\hat{X}_0^N$ and $\hat{\tilde{X}}^N$ by fast Fourier transforms. The linear eigenvalue problem (2.5) is thus approximated by

$$\lambda \hat{\tilde{X}}^N = \hat{L}^N \hat{\tilde{X}}^N. \tag{A 1}$$

Here, $\hat{L}^N$ is a square matrix of dimension $3N$ whose coefficients are given by the formula

$$\hat{L}_{i,j}^N = \left\{ FFT_N \left[ \mathcal{L}_{\varphi,k_z} \left( X_0^N; \varphi, k_z \right) FFT_N^{-1} E_j^N \right] \right\}_i, \tag{A 2}$$

where $E_j^N$ are the vectors of the canonical basis of $\mathbb{C}^{3N}$, and where $FFT_N$ and $FFT_N^{-1}$ refer to the direct and inverse discrete Fourier transforms. A pseudo-spectral
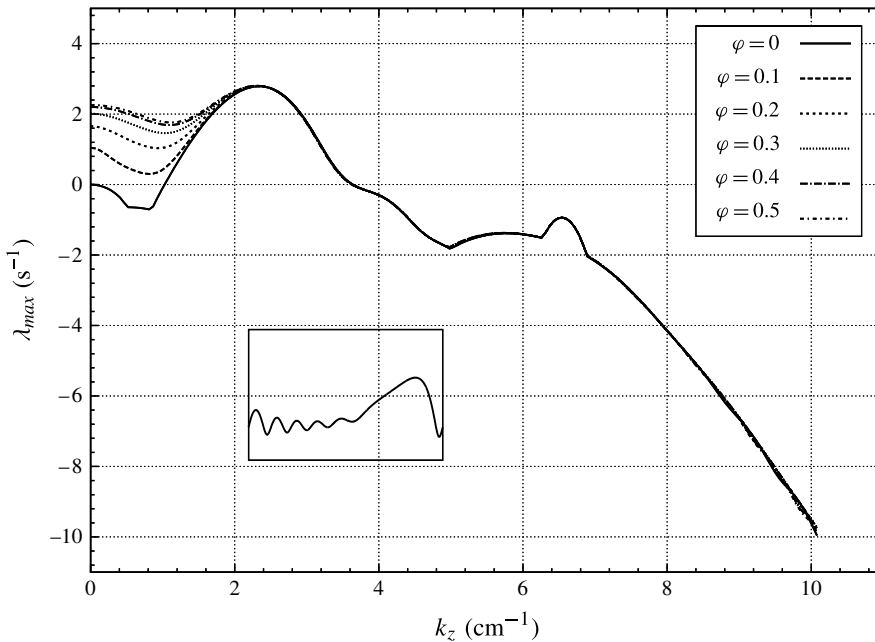
FIGURE 18. Same as figure 17 except for $\beta = 10.1°$, $Re = 41$, $f = 5.3$ Hz.

algorithm is next invoked, convolutions being easily computed in the physical space and derivatives in the Fourier space. A drawback of this procedure is the aliasing problem. To take care of it, we actually apply (A 2) on a four times finer grid:

$$\hat{\boldsymbol{L}}_{i,j}^{N} \approx \left\{ FFT_{4N} \left[ \mathscr{L}_{\varphi,k_z} \left( \boldsymbol{X}_0^{4N}; \varphi, k_z \right) FFT_{4N}^{-1} E_j^{4N} \right] \right\}_i . \tag{A 3}$$

The 2D base solution is approximated on the finer grid by taking the inverse Fourier transform of $\hat{X}_0^{4N}$ where the coefficients corresponding to the highest frequencies, that is three-quarters of the total number, are set to zero.

Figure 17 compares the growth rate of the most dangerous mode for $\varphi = 0$ computed on a fine grid ($N = 2048$) and a coarser one ($N = 1024$). Parameters correspond to a typical $\gamma_2$ solitary-like wave-train running on a water film. Convergence is already reached on a $N = 1024$-node regular grid and most of the results presented in this paper have been obtained with $N = 1024$.

The influence of the detuning parameter $\varphi$ on the results has been tested for six different values of $\varphi$ in the range [0, 1/2] which is sufficient to cover all possible perturbations for symmetry reasons. The results are shown in figure 17 for an isolated quasi-solitary wave. No noticeable effects of the detuning parameter on the maximum growth rate have been found, except for very long-wave perturbations $k_z \ll 1$ where small differences between the curves can be noted. However, these differences are not significant. Yet, wherever the wave is non-isolated, the detuning parameter has a significant effect on its stability. The most amplified 2D perturbation ($k_z = 0$) is sensitive on the detuning parameter, i.e. on the extension of the considered wave train (see figure 18). However, the transverse stability ($k_z \neq 0$) remains unaffected by the detuning parameter. We may then conclude that the stability of a single $\gamma_2$ wave and the stability of an infinite train of these waves are equivalent.

## Appendix B. Kinetic energy budget

The different terms which compose the right-hand side of the kinetic energy budget (2.11) are listed in table 2. They are grouped with respect to their physical origin: inertia forces, hydrostatic pressure, viscous drag at the wall, 'Trouton' second-order viscous dispersion terms, capillarity (surface tension). We first present the terms emanating from the projection of the momentum balance in the streamwise direction, referred below as '*q*-' contributions. The contributions from the spanwise projection of the momentum balance, or '*p*-' terms come next.

### REFERENCES

ALEKSEENKO, S. V., NAKORYAKOV, V. Y. & POKUSAEV, B. G. 1985 Wave formation on a vertical falling liquid film. *AIChE J.* **31**, 1446–1460.

ALEKSEENKO, S. V., NAKORYAKOV, V. E. & POKUSAEV, B. G. 1994 *Wave Flow in Liquid Films*, 3rd edn. Begell House.

ALLEN, R. F. 1975 The role of surface tension in splashing. *J. Colloid Interface Sci.* **51** (2), 350–351.

BAKOPOULOS, A. 1980 Liquid-side controlled mass transfer in wetted-wall tubes. *Ger. Chem. Engng* **3**, 241–252.

BALMFORTH, N. J. & LIU, J. J. 2004 Roll waves in mud. *J. Fluid Mech.* **519**, 33–54.

BENJAMIN, T. B. 1957 Wave formation in laminar flow down an inclined plane. *J. Fluid Mech.* **2**, 554–574.

BO, S., MA, X., LAN, Z., CHEN, J. & CHEN, H. 2010 Numerical simulation on the falling film absorption process in a counter-flow absorber. *Chem. Engng J.* **156**, 607–612.

CHANG, H. C., DEMEKHIN, E. A. & KOPELEVITCH, D. I. 1993 Nonlinear evolution of waves on a vertically falling film. *J. Fluid Mech.* **250**, 433–480.

CHENG, M. & CHANG, H. C. 1995 Competition between subharmonic and sideband secondary instabilities on a falling film. *Phys. Fluids* **7** (1), 34–54.

DEMEKHIN, E. A. & KALAIDIN, E. N. 2007 Three-dimensional localized coherent structures of surface turbulence. I. Scenarios of two-dimensional-three-dimensional transition. *Phys. Fluids* **19**, 114103.

DEMEKHIN, E. A., KALAIDIN, E. N., KALLIADASIS, S. & VLASKIN, S. Y. 2007 Three-dimensional localized coherent structures of surface turbulence. II. $\lambda$ solitons. *Phys. Fluids* **19**, 114104.

DEMEKHIN, E. A., KALAIDIN, E. N. & SELIN, A. S. 2010 Three-dimensional localized coherent structures of surface turbulence. III. Experiment and model validation. *Phys. Fluids* **22**, 092103.

DIETZE, G. F., AL-SIBAI, F. & KNEER, R. 2009 Experimental study of flow separation in laminar falling liquid films. *J. Fluid Mech.* **637**, 73–104.

DIETZE, G. F., LEEFKEN, A. & KNEER, R. 2008 Investigation of the backflow phenomenon in falling liquid films. *J. Fluid Mech.* **595**, 435–459.

DOEDEL, E. J. 2008 *Auto07p continuation and bifurcation software for ordinary differential equations*. Montreal Concordia University.

FRISK, D. P. & DAVIS, E. J. 1972 The enhancement of heat transfer by waves in stratified gas–liquid flow. *Intl J. Heat Mass Transfer* **15**, 1537–1552.

FUJITA, T. 1993 Falling liquid films in absorption machines. *Intl J. Refrig.* **16**, 282–294.

GERMAIN, P. 1973 *Cours de Mécanique des Milieux Continus*. Masson.

HEINING, C., POLLAK, T. & AKSEL, N. 2012 Pattern formation and mixing in three-dimensional film flow. *Phys. Fluids* **24**, 042102.

KALLIADASIS, S., RUYER-QUIL, C., SCHEID, B. & VELARDE, M. G. 2012 *Falling Liquid Films*. Springer.

KRECHETNIKOV, R. 2009 Rayleigh–Taylor and Richtmyer–Meshkov instabilities of flat and curved interfaces. *J. Fluid Mech.* **625**, 387–410.

LEONTIDIS, V., VATTEVILLE, J., VLACHOGIANNIS, M., ANDRITSOS, N. & BONTOZOGLOU, V. 2010 Nominally two-dimensional waves in inclined film flow in channels of finite width. *Phys. Fluids* **22**, 112106.

LIU, J. & GOLLUB, J. P. 1994 Solitary wave dynamics of film flows. *Phys. Fluids* **6**, 1702–1712.

LIU, J., SCHNEIDER, J. B. & GOLLUB, J. P. 1995 Three-dimensional instabilities of film flows. *Phys. Fluids* **7** (1), 55–67.

MARMOTTANT, P. & VILLERMAUX, E. 2004 On spray formation. *J. Fluid Mech.* **498**, 73–111.

MOISY, F., RABAUD, M. & SALSAC, K. 2009 A synthetic schlieren method for the measurement of the topography of a liquid interface. *Exp. Fluids* **46** (6), 1021–1036.

ORON, A., GOTTLIEB, O. & NOVBARI, E. 2007 Bifurcations of a weighted-residual integral boundary-layer model for nonlinear dynamics of falling liquid films. *J. Phys.: Conf. Ser.* **64** (1), 012007.

PARK, C. D. & NOSOKO, T. 2003 Three-dimensional wave dynamics on a falling film and associated mass transfer. *AIChE J.* **49** (11), 2715–2727.

RASTATURIN, A., DEMEKHIN, E. & KALAIDIN, E. 2006 Optimal regimes of heat-mass transfer in falling film. *J. Non-Equilib. Thermodyn.* **31**, 1–10.

RAYLEIGH, L. 1883 Investigation of the character of the equilibrium of an incompressible heavy fluid of variable density. *Proc. Lond. Math. Soc.* **14**, 170–177.

RIBE, N. M. 2001 Bending and stretching of thin viscous sheets. *J. Fluid Mech.* **433**, 135–160.

RUYER-QUIL, C. 1999 Dynamique d'un film mince s'écoulant le long d'un plan incliné. PhD thesis, École Polytechnique, LadHyx, France.

RUYER-QUIL, C. & MANNEVILLE, P. 2000 Improved modeling of flows down inclined planes. *Eur. Phys. J.* B **15**, 357–369.

SCHEID, B., KALLIADASIS, S., RUYER-QUIL, C. & COLINET, P. 2008 Interaction of three-dimensional hydrodynamic and thermocapillary instabilities in film flows. *Phys. Rev. E* **78**, 066311.

SCHEID, B., RUYER-QUIL, C. & MANNEVILLE, P. 2006 Wave patterns in film flows: modelling and three-dimensional waves. *J. Fluid Mech.* **562**, 183–222.

SCHEID, B., RUYER-QUIL, C., THIELE, U., KABOV, O. A., LEGROS, J. C. & COLINET, P. 2005 Validity domain of the Benney equation including the Marangoni effect for closed and open flows. *J. Fluid Mech.* **527**, 303–335.

SCHLICHTING, H., GERSTEN, K. & KRAUSE, E. 2004 *Boundary-Layer Theory*, 8th edn Springer.

SHKADOV, V. YA. 1967 Wave flow regimes of a thin layer of viscous fluid subject to gravity. *Izv. Akad. Nauk, SSSR Mekh. Zhidk. Gaza* **1**, 43–51; English translation in *Fluid Dyn.* **2**, 29–34, 1970 (Faraday Press, NY).

SHKADOV, V. YA. 1977 Solitary waves in a layer of viscous liquid. *Izv. Akad. Nauk SSSR Mekh. Zhidk. Gaza* **1**, 63–66.

SHKADOV, V. YA. & SISOEV, G. M. 2004 Waves induced by instability in falling films of finite thickness. *Fluid Dyn. Res.* **35**, 357–389.

SKOTHEIM, J. M., THIELE, U. & SCHEID, B. 2003 On the instability of a falling film due to localized heating. *J. Fluid Mech.* **475**, 1–19.

SPAID, N. & HOMSY, G. 1996 Stability of Newtonian and viscoelastic dynamic contact lines. *Phys. Fluids* **8**, 460–478.

TAYLOR, G. I. 1950 The instability of liquid surfaces whan accelerated in a direction perpendicular to their planes. Part 1. Waves on fluid sheets. *Proc. R. Soc. Lond.* **201**, 192–196.

VLACHOGIANNIS, M., SAMANDAS, A., LEONTIDIS, V. & BONTOZOGLOU, V. 2010 Effect of channel width on the primary instability of inclined film flow. *Phys. Fluids* **22**, 012106.

YOSHIMURA, P. N., NOSOKO, T. & NAGATA, T. 1996 Enhancement of mass transfer by waves into a falling laminar liquid film by two-dimensional surface waves – some experimental observations and modeling. *Chem. Engng Sci.* **51**, 1231–1240.